
Unterschrift (Betreuer)



TECHNISCHE
UNIVERSITÄT
WIEN

Vienna University of Technology

MASTER THESIS

Development of a LA-ICP-MS procedure for the spatially resolved analysis of fly ash particles

ausgeführt am Institut für
Chemische Technologien und Analytik
der Technischen Universität Wien

unter der Anleitung von
Associate Prof. Dipl.-Ing. Dr.techn. Andreas Limbeck
und
Dipl. Ing. Gerald Bauer

durch
Birgit Achleitner, BSc
Tichtelgasse 16/7
A-1120 Wien

Datum

Unterschrift (Student)

Abstract

Fly ash and other solid residues are accumulated during every combustion process. The main sectors of industry responsible for the production of incineration waste are: (1) municipal waste incineration and co-incineration of waste in other combustion plants, (2) coal-fired and biomass power plants, (3) the metal producing industry and (4) the cement industry. In addition to the raw material, the combustion technology, operating parameters and the type of emission control system define the properties of the formed ashes. Due to their chemical composition, incineration residues are often considered waste and deposition in landfills is the only possibility.

Recycling and reuse of combustion waste poses an alternative and is forced through elevated disposal costs, shrinking availability of landfill space and stricter environmental regulations. If legal standards concerning chemical composition are met, incineration residues are used in the cement and concrete production, in the glass and ceramic industry, for road pavements, in agriculture etc. Furthermore, the resource recovery from waste (urban mining or landfill mining) has become an interesting subject over the past few years. The economic feasibility is hereby of major importance and depends on many factors like the available process technology and the situation on the metal market. Consequently, a careful investigation of certain waste fractions is necessary. Although a lot of information regarding particle composition is available, the spatial distribution of elements within a particle is hardly known.

During this work, a method to gain insight into the structure of a single ash particle was developed and the creation of elemental images was fostered using LA-ICP-MS in combination with SEM-EDX. Two different kind of ashes, one obtained from the municipal waste incinerator in Spittelau (Vienna), the other from a blast furnace (voestalpine, Linz) were investigated. First, samples were prepared using a novel sample preparation

technique to swirl up a fly ash sample and disperse the particles on a sample carrier. After fixation, LA-ICP-MS allowed the spatially resolved analysis of an isolated specimen. In general, particles with diameters between 60 - 120 μm were selected for analysis. By preparing a cross-section and then scanning the received surface of a single fly ash particle with the laser, the distribution of certain elements was recorded. The aim was to identify shell and core-enriched analytes and visualize the results. Two different approaches of gaining information about elemental distribution were introduced: fast scanning by using only one laser pattern and detailed surface analysis by recording several adjoined laser pattern. The main components as well as the surface structure were analyzed using SEM-EDX. Additionally, EDX mappings served as reference for LA-ICP-MS method validation. Data obtained from both techniques was processed using the ImageLab software. Images with a resolution of 24 x 24 px or 40 x 40 px were obtained depending on the beam diameter and the selected imaging area. By combining information from both measurements a detailed characterization of the fly ash samples was possible.

Concerning the two introduced fly ash samples, it was found out that Ca, O, Si and Al formed the basis of FLA fly ash while Ti, Zn, Sn, Sb and Pb were only present in certain particle structures. HZ9 contained iron-based and carbon-based particles. While Al and Ti were found incorporated into carbon particles, iron-based specimen exclusively exhibited surface-enriched analytes like Ti, Mn, Zn and Pb.

Kurzfassung

Feste Rückstände, unter anderem auch Flugasche, fallen bei jedem Verbrennungsprozess an. Die größten Verursacher sind hierbei auf wenige Industriezweige beschränkt: (1) Anlagen zur Abfallverbrennung insbesondere Müllverbrennungsanlagen und Feuerungsanlagen in denen Abfälle mitverbrannt werden, (2) Kohle- und Biomasse(heiz)kraftwerke (3) Feuerungsanlagen in der Metallindustrie und (4) Anlagen in der Zementindustrie. Abgesehen von der Art des eingesetzten Rohstoffes wird die chemische Zusammensetzung der Rückstände maßgeblich von der Art der Feuerungsanlage, den Betriebsparametern und dem implementierten Abgasreinigungssystem bestimmt. Aufgrund des meist hohen Schadstoffgehaltes gelten Verbrennungsrückstände als Abfall und werden deponiert, wobei strengere Umweltauflagen und der Mangel an geeigneten Deponiestandorten zu erhöhten Kosten für die Deponierung führen.

Werden gesetzliche Grenzwerte eingehalten, stellt das Recycling von bestimmten Aschefractionen eine Alternative dar. Die Verwendung von Verbrennungsrückständen in der Zementindustrie, bei der Herstellung von Keramiken, als Düngemittel in der Landwirtschaft, usw. sind heutzutage weit verbreitet. Auch die Wertstoffrückgewinnung aus Abfällen (Urban Mining oder Landfill Mining) spielt eine immer größer werdende Rolle. Die wirtschaftliche Umsetzbarkeit in Abhängigkeit von der verfügbaren Prozesstechnologie, der Situation am Weltmarkt und der geforderten Produktqualität ist hier der entscheidende Faktor. Infolgedessen ist auch eine genaue Charakterisierung geeigneter Abfallfraktionen nötig. Informationen zur Zusammensetzung von Verbrennungsrückständen sind in großer Zahl vorhanden und behandeln den Fluss von Metallen und anderen Substanzen während der Verbrennung und deren ökologischen Auswirkungen. Informationen über die räumliche Verteilung von Analyten sind allerdings nur wenig vorhanden, obwohl diese für die Entwicklung einer möglichen Recycling-Strategie eben-

so von Bedeutung sind.

Im Zuge dieser Arbeit wurde deshalb eine Methode entwickelt um die Struktur und die Verteilung von Elementen innerhalb eines einzelnen Flugaschepartikels darzustellen. Zwei unterschiedliche Proben wurden analysiert um Unterschiede in der Zusammensetzung herausarbeiten zu können: Flugasche aus einer Müllverbrennungsanlage (Spittelau, Wien) und Flugasche gesammelt im Abgasreinigungssystem eines Hochofens (voestalpine, Linz). Mithilfe einer selbst-entwickelten Prozedur zur Probenvorbereitung wurde in einem ersten Schritt die Flugasche als isolierte Partikel auf einem präparierten Probenträger aufgebracht. LA-ICP-MS erlaubte im Anschluss die orts aufgelöste Untersuchung von einzelnen Partikelquerschnittsflächen mit dem Ziel Elemente mit unterschiedlichem Vorkommen innerhalb der Oberfläche zu identifizieren und darzustellen. Zwei unterschiedliche Messmethoden wurden hierzu entwickelt: das schnelle Überprüfen einer Querschnittsfläche durch nur eine Lasermessung und die detaillierte Analyse durch mehrere, nebeneinanderliegende Lasermuster. Partikel mit einem Durchmesser von 60 - 120 μm wurden dazu ausgewählt. Mittels SEM-EDX erfolgte die Darstellung von Partikelstrukturen und die Identifizierung der Hauptkomponenten. Außerdem dienten Elementarverteilungen aus EDX-Messungen als Referenz um die LA-ICP-MS Methode zu verifizieren. Die Daten aus beiden Messmethoden wurden anschließend kombiniert um eine umfassende Beschreibung der Aschepartikel zu ermöglichen. Die Datenauswertung erfolgte mit Hilfe der ImageLab Software wobei Images mit einer Auflösung von 24 x 24 px bzw. 40 x 40 px erhalten wurden, je nach Laserdurchmesser und der Gesamthöhe und -breite der abgerasterten Fläche.

Bezogen auf die beiden vorgestellten Flugascheproben ergab sich Folgendes: Ca, O, Si und Al bildeten das Gerüst der FLA Probe und Ti, Zn, Sn, Sb, und Pb waren nur in bestimmten Strukturen zu finden. Im Gegensatz dazu, bestand die HZ9 Probe aus Eisen und Ruß-Partikeln. Während Al und Ti im Inneren der Rußproben zu finden waren, waren Ti, Mn, Zn und Pb nur an der Außenseite der Eisenpartikel vorhanden.

Danksagung

Zuallererst möchte ich mich bei meinem Betreuer Assoc. Prof. Andreas Limbeck für die ausgezeichnete Unterstützung bedanken. Seine zahlreichen Ratschläge und das wertvolle Feedback haben mich motiviert und stets bestärkt in meiner Arbeit.

Dank gebührt außerdem Gerald Bauer für die Bereitstellung des interessanten Themas und der Hilfestellung bei der praktischen Durchführung sowie dem Rest der Arbeitsgruppe Limbeck für das positive und lockere Arbeitsklima. Besonderer Dank gilt hierbei auch Max Bonta der durch seinen Enthusiasmus und seine Imaging-Erfahrung eine große Hilfe war.

Weiters möchte ich mich bei Elisabeth Eitenberger bedanken, die mit mir zahlreiche Stunden vor dem REM verbrachte und mich bei der Charakterisierung meiner Proben unterstützte als auch Prof. Johann Lohninger für die Bereitstellung der ImageLab Software und sein großes Entgegenkommen bei der Datenauswertung.

Vielen Dank ebenfalls an Assoc. Prof. Johann Fellner vom Institut für Wassergüte, Ressourcenmanagement und Abfallwirtschaft (E226) sowie Peer Ole Mallow und Verena Trinkel für die Bereitstellung der Proben und den fakultätsübergreifenden Austausch.

Abschließend möchte ich mich noch bei meiner Familie bedanken, die nicht nur während meines Studiums stets eine Stütze und ein Rückzugsort für mich war. Vielen Dank!

Contents

Abstract	ii
Kurzfassung	iv
Danksagung	vi
1 Introduction	1
2 Theoretical Aspects	3
2.1 Solid combustion residues	3
2.1.1 Formation of solid waste during combustion	4
2.1.2 Chemical composition and environmental impact	6
2.1.3 Application and recycling strategies	7
2.2 Inductively coupled plasma mass spectrometry (ICP-MS)	9
2.2.1 Sample introduction	9
2.2.2 Plasma source	11
2.2.3 Interface region	13
2.2.4 Ion optics	14
2.2.5 Ion separation	14
2.2.6 Detection	17
2.3 Laser ablation coupled to an ICP-MS	17
2.3.1 Instrumentation	19
2.3.2 Operating parameters	20
2.4 Scanning electron microscopy (SEM)	21
2.4.1 Instrumentation	22
2.4.2 Electron-sample interactions	23

3	Experimental	26
3.1	Instrumentation	26
3.2	Sample characterization	27
3.3	Sample preparation	28
3.3.1	Particle dispersion	28
3.3.2	Deposition strategy	28
3.3.3	Verification strategy	29
3.4	Laser ablation experiments	30
3.4.1	Preparation of cross-section areas	30
3.4.2	Linescan measurements and operating conditions	31
3.4.3	Image creation and optimization	32
3.5	Method validation using SEM-EDX	33
4	Results and Discussion	34
4.1	Sample preparation	34
4.2	Realization and optimization of pre-ablation	38
4.3	Linescan measurements	39
4.3.1	Realization and optimization of linescan measurements	39
4.3.2	Detailed particle analysis through linescan measurements	44
4.3.3	Sample characterisation and résumé	47
4.4	Image measurements	49
4.5	Method validation using SEM-EDX	52
4.6	FLA sample characterisation	58
4.7	HZ9 sample characterisation	64
5	Conclusion	68
5.1	Method development and optimization	68
5.2	Sample characterisation	72
6	Outlook	74

1 Introduction

Solid residues are produced during every combustion process and are of major importance for various reasons. Accumulated refuse in the form of bed and fly ash poses a risk to human health and the environment due to a high content of heavy metals, organic pollutants and salt. As a result, residues from air pollution control (APC) are classified as waste according to the European Waste Catalogue.[1] In practice, these substances are deposited in landfills. Due to stricter environmental regulations and shrinking availability of landfill space, escalating disposal costs are anticipated. In addition, if not properly disposed, fly ash and other slags can cause water and soil pollution.[2]

If legal standards are met, recycling and reuse of incineration waste poses an alternative. In the metal industry, internal recycling and the recovery of certain metals and associated materials is done.[3] Other possible applications are the cement and concrete production, road pavements, the glass and ceramic industry, agriculture and the adsorbent and zeolite production where residues from coal and biomass power plants and from municipal waste incinerators are processed. Numerous papers discuss benefits and drawbacks of these strategies ([4],[5],[6],[7]).

Additionally, the resource recovery from waste, also from incineration residue has become an interesting subject over the past years. Urban mining and landfill mining are concepts engaging in diversifying metal resources, especially for precious and rare earth metals. The challenge hereby is to identify and concentrate metals in particular fractions of incinerator waste and then estimate the economic feasibility of a recovery. The development of possible recycling strategies depends strongly on the product quality requirement, the situation on the metal market, energy prices and the available process technology.[8][9][10]

As a consequence, a careful investigation of combustion residues is necessary in any of the above mentioned cases. Even for the disposal into ash ponds or landfills, characterisation of the long-term behavior, the concentration and leaching properties of heavy metals, the amount of incorporated organic pollutants etc. is required. As a result, a lot of information regarding particle composition and the flux of elements within a combustion process is available ([11],[12],[13],[14]). In order to develop a recycling strategy even more detailed analysis is necessary. The analytes of interest need to be identified, quantified and characterized regarding their state (oxide, sulfate, silicate, etc.) and their distribution among a single particle. Surface enriched elements can be easily accessed and recovered compared to core enriched substances but spatial distribution of elements in fly ash particles is mostly unknown.

Hence, the aim of this work was to gain access to internal structures and the distribution of certain analytes within a single fly ash particle. This includes the development of a suitable sample preparation strategy, the method development to identify accumulations of certain elements and finally, the visualization of elemental distributions throughout a particles' surface.

First of all, sample preparation is necessary to allow analysis of single fly ash particles. Hereby, the representative application of all present particle sizes and adequate fixation on a sample carrier without the formation of agglomerates or bursting of particles is essential.

Secondly, a LA-ICP-MS method has to be introduced to determine elemental distributions. ICP-MS was the method of choice offering several benefits like the determination of elements at a trace or ultratrace level and the direct analysis of solid samples in combination with laser ablation. Consequently, the spatially resolved analysis of small structures like an isolated fly ash particle is possible.

Based on former studies on the chemical composition of fly ash (e.g. [15],[8],[16]), a classification of particles into samples exhibiting a core-shell structure and samples without a core-shell structure was suggested. Thus, the overall goal was to identify shell- and core-enriched elements and visualize their distribution.

2 Theoretical Aspects

2.1 Solid combustion residues

In addition to emissions into air and water, solid residues are accumulated during every combustion process in various industries. The properties of the formed ashes depend on the raw material, the combustion technology and operating parameters as well as the type of emission control system implemented into the process.[2] In addition to the generation of combustion waste, residues and slag or ash from other industries are usually utilized in incinerators.

The main sectors of industry responsible for the production of solid residues are

- municipal waste incineration

In a municipal waste incineration plant the combustion of consumer waste and industrial or commercial refuse similar to domestic waste takes place. Further matured forest, animal meal, sewage sludge, plastic waste, oil residues, etc. is burnt. Refuse incineration plants serve as secured sinks for hazardous substances. Even at the highest pollution input, a complete destruction of organic contaminants, concentration of thermally non-destructive pollutants and low emissions have to be ensured.[2] Benefits of waste combustion are the reduction of garbage volume and mass, the destruction of organic pollutants and the use of energy incorporated into waste through the transformation into electricity and heat.[5]

- co-incineration of waste in combustion plants

Plants that produce energy or manufacture products, including power plants, the pulp and paper industry, the wood and cement industry, often incinerate waste. Sewage sludge, animal meal, swarf, leather waste and others are burnt if the origin, composition and hazardous properties correspond to legal standards. The pri-

mary goal hereby is to cover the energy demand on site and to utilize and recycle production residues.[2]

- power plants

Solid waste is produced in coal-fired power plants and biomass combustion plants.[4]

- metal producing industry

Solid residues produced in the iron and steel industry are in large part recycled internally by recirculation into the blast furnace or sintering plant. The use of recycled iron improves the iron and steel making process due to a high content of CaO and MnO. A high recycling rate means reduction of waste but also increases the risk of unwanted accumulation of elements especially heavy metals. As a consequence product quality might be decreased. Slag from the blast furnace and steel slag have also found a wide application outside the metal industry, e.g. cement industry, road construction, fertilizer production and so on. Additionally, nonferrous metal industry combustion processes produce solid waste, mainly the secondary aluminium and copper industry. The recovery/treatment of salt slag from secondary aluminium production to recycle Al and salt is important to reduce the landfilling costs and the environmental impact. Copper slag is used to recover Cu, Ni and Co.[3]

- cement industry

In the cement industry, ashes and residues from other industries, in particular metal industry and power plants, are used as secondary raw material. To an increasing extent, oil residues, used tires, plastic waste and other refuse are used as combustible material. As all formed solid residues are reused internally, no additional solid waste is produced.[2]

2.1.1 Formation of solid waste during combustion

Solid waste accumulates at various points within the combustion process.

Picture 2.1 shows a schematic illustration of a municipal waste incineration plant with grate firing typically used for the combustion of urban waste. Alternative technologies used are fluidized bed combustion to utilize slurries and the rotary furnace which can

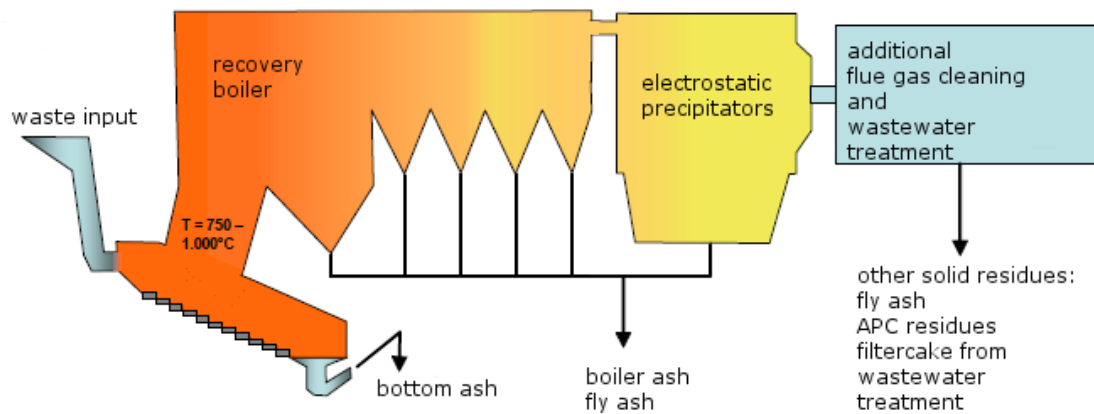


Figure 2.1: Formation of solid residues within the waste incineration process [2]

be used to dispose hazardous waste.[2] During incineration the waste is fed continually into the combustion chamber. To enhance the combustion high temperatures (at least 850°C) are applied, as well as increased turbulence and a longer flue gas residence time to elevate burnout. To prevent the formation of dioxins and carbon monoxide a sufficient air supply must be ensured. A recovery boiler is implemented downstream to produce steam and as a consequence electric energy from the generated heat. Environmental compliance is accomplished by an air pollution control system.[5]

Bottom ash is formed in the combustion chamber through sintering of silicates and aluminum oxide incorporated in waste as well as softening of slag-forming glasses. In grate firings and rotary furnaces, bottom ash is removed and cooled at the end of the chamber. In fluidized bed combustion, ash can be deposited with cyclones. Coarse, swirled up particles settle in the recovery boiler while a fine portion of particles, named fly ash as well as acid gases and trace quantities of uncombusted or uncombustible volatilized pollutants are carried on further via the flue gas. The separation of fly ash is done by different filtering techniques. Depending on additional flue gas cleaning systems other solid residues might occur, referred to as residues from air pollution control (APC).[1]

In coal-fired power plants or biomass combustion plants similar categories of solid waste are obtained: bottom ash, fly ash, residues from desulfurization and filter cake from wastewater purification.

In the metal industry manufacturing takes place in large, complex sites with many

single process steps. Bed ash originating from various locations, e.g. blast furnace, oxygen converter, slurries from wastewater treatment and rolling mills, fly ash from flue gas cleaning etc. occur.[2]

2.1.2 Chemical composition and environmental impact

The composition of obtained ashes varies primarily due to the raw material and type of combustion process. Furthermore, different elements and phases show different properties e.g. boiling points which reflect on the elemental composition of certain ash fractions.

Bottom ash from municipal waste incineration mostly consists of calcium oxide and aluminosilicate compounds alongside with unburnt organic matter and metals with low volatility.[2]

Fly ash and other residues from air pollution control (APC) contain mineral and metallic substances and soot. Due to the nature of the surface of the ash particle and the overall high surface area the adsorption of metals with high volatility, acids and other organic substances occurs. Primary factors which determine the presence of metals in APC residues are the boiling points of different phases.[8] Elements were classified by Klein et al [15] due to their accumulation in fly ash:

- Elements with high boiling points (e.g. Al, Ca, Fe, K, Si, Ti, . . .) form the basis of the fly ash. They are not volatilized but can be transported in the form of small particles or droplets.
- Elements like As, Cd, Cu, Pb, Zn, . . . are volatilized during incineration but condensate on the fly ash particles during flue gas treatment.
- Hg, Cl, Br and others are volatilized but remain in the gas phase.
- Elements with mixed behaviour exist, e.g. Cr, Ni, . . .

Additionally, the thermodynamic stability of formed metal oxides and chlorides plays an important role. If the metal oxide is more stable than the chloride, the element is found in the matrix of the ash particle because it is transported mechanically. If the metal

chloride is more stable than the oxide, the metal chloride volatilizes and condenses on the surface of the particle.[16]

The type of waste combusted, its content of chlorine, sulfur and water, the oxidation level, temperature, processing time and the boiling points of different phases yield in the presence of elements in specific species and their concentration in fly ash. In spite of different pollution control devices, different geographic locations and varying waste inputs, the composition of APC residues is broadly consistent across different facilities. Because of the high concentration of metals, soluble salts and toxic organic pollutants, APC residues are classified as waste according to the European Waste Catalogue.[1][12]

Aside from municipal waste combustion the composition of residues strongly depends on the type of material processed. In coal-fired power plants the chemical characteristics of residues are influenced by geological factors related to the coal deposits. The content of heavy metals for example is significantly affected by the coal quality.[4] Fresh wood in biomass combustion plants only possesses a low amount of heavy metals but also a low ash content, resulting in higher concentration of heavy metals in incineration residues. In metal industry, the main content of the solid residues is the metal used wherefore internal recycling is possible. Nevertheless concentration of unwanted species occurs and may lead to poor product quality if not carefully monitored.[2]

2.1.3 Application and recycling strategies

In practice, residues from incineration processes are mainly used as construction material or reused by recirculation as in the metal industry. Otherwise combustion residues are considered waste and are deposited in landfills. The release of metals or harmful substances from landfills poses a risk to water quality, soil quality and human health and has to be prohibited. In this context, the disposal of bottom ash is considered less problematic than the disposal of fly ash. [2][3]

Depending on the type of disposal/application various threshold values have to be met. In order to decrease the mobility of pollutants or remove them from the waste fraction different post-treatment processes are available. Basically, they can be divided into

three categories. Through separation processes like washing, leaching, electrochemical processes and/or mechanical processes specific substances or size ranges can be separated. Solidification and stabilization uses binders or additives like cement to chemically or physically immobilize hazardous content. Thermal methods like vitrification reduce the solubility of pollutants as well and are also used to destroy organic contaminants. [5]

If legal standards are met, fly ash and slags are used as additives in cement, for the backfilling of opencast mines, for road construction, in the ceramic industry and so on. Residues from biomass combustion plants can be used as fertilizers if untreated biomass was used. Recovery of certain metals from metal slag is done in the metal industry.

Although a range of applications is possible, the reuse of incineration waste is limited by high concentrations of heavy metals, salts and others pollutants.[2][3] Therefore resource recovery from waste, also from incineration residue, has become an interesting subject over the past years. Precious metals and rare earth metals, which are increasingly used in modern high-technology industries, have limited natural resources, are unevenly distributed and their prices fluctuate. Urban mining (recycling of annual waste flows) and landfill mining (recovery of deposited materials from landfills) are concepts engaging in diversifying metal resources. [8][9]

The occurrence of strategically important metals in combustion residues has been investigated in literature ([1],[9],[17],[18]). Concentrations of In and Ag have been found to be higher than the average crustal abundance but lower than present ore concentrations. Also the concentration of rare earth elements was found to be low.[1] Morf et al reported that more than 80 % of the total economical potential of waste residues in a Swiss incineration plant are associated with only 7 investigated metals: Au, Sc, Al, Cu, Ag, Pt and Nd. Not only economic aspects have been considered, but also the environmental impact caused by the primary production of metals. The goal for further developments is to concentrate precious metals in particular fractions of incinerator waste and then estimate the economic feasibility of a recovery. The strategies depend on the product quality requirement, the situation on the metal market, energy prices and available process technology. Concentration and storage for later reuse would be a possibility as well. [9]

2.2 Inductively coupled plasma mass spectrometry (ICP-MS)

Inductively coupled plasma (ICP) mass spectrometry is a versatile tool for determining elements at a trace or ultratrace concentration level with a broad dynamic range and good precision. It is used for all kinds of samples and offers the possibility of determining isotope ratios and abundances of isotopes. A drawback of this technique is the occurrence of isobaric interferences, limiting the analysis of certain elements.[19]

In ICP-MS, the sample is converted into an aerosol and transported into the plasma where the ionization occurs. Ions are extracted via a low-pressure interface and then focused by an ion lens system into a high-vacuum mass analyzer. A simple scheme of an ICP-MS is shown in figure 2.2 whereat individual components will be discussed in the following chapters.

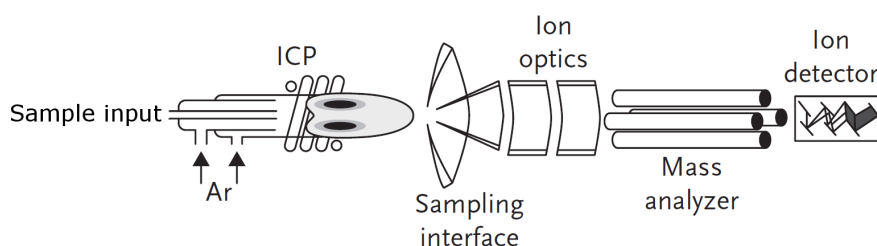


Figure 2.2: Principal components of a quadrupole ICP-MS system [20]

2.2.1 Sample introduction

A variety of systems exist to introduce gas, liquid or solid samples into an inductively coupled plasma mass spectrometer. Analyzing a sample in its natural state would be the best [21]. Due to the multitude of methods only a brief summary should be given here.

Gaseous sample introduction

An approach for transporting samples into the plasma is through the gas phase. A high transport efficiency and a decrease of matrix interferences are the main benefits. However, the analytes of concern are often not easily converted to the gaseous state.

Methods for introducing a gaseous sample are the coupling of the ICP-MS with a gas

chromatographic system or the direct introduction of the analytes via the injector gas flow. [21]

Liquid sample introduction

Liquid sample introduction through a nebulizer and a spray chamber is the most commonly used sample introduction system today. In a first step, liquids are dispersed into a fine aerosol using a nebulizer. Before entering the plasma, large droplets are removed from the aerosol stream via a spray chamber. Many different designs regarding nebulizers and spray chambers are available. Nebulizers are usually made from glass or various kinds of polymer especially for highly corrosive samples. Pneumatic nebulizers are widely spread, using the mechanical force of a gas stream to generate the sample aerosol. The main tasks of a spray chamber are to only allow small droplets to enter the plasma and to smooth out pulses that occur during the nebulization process. To increase thermal stability of the sample and minimize the amount of solvent loading some spray chambers are externally cooled.

Special methods for introducing a liquid sample are electrothermal vaporization (ETV) of a liquid droplet or hydride generation. The latter is used to analyze elements that form volatile hydrides e.g. As, Bi, Ge, Pb, Sb, Se, Sn and Te. The sample is converted in a chemical reaction where volatile compounds are formed. During this process a separation of analytes from the sample matrix occurs reducing the potential of spectral interferences. [21]

Solid sample introduction

Introducing a solid sample is achieved by a variety of techniques offering several advantages over liquid sample introduction. First of all, sample preparation time and the likelihood of contaminations due to sample preparation is reduced. In addition, spectral interferences derived from solutions are absent and certain methods provide spatially resolved information. On the other hand quantitative analysis is limited due to the lack of solid standards.

Insertion of solid samples can be performed via direct insertion devices or by generating an aerosol or vapor from arc and spark ablation, laser ablation and electrothermal

vaporization (ETV).[21] ETV is a sample introduction method suitable for liquid and solid samples. The sample is put in a graphite furnace or on a tungsten or tantalum filament which is electrothermally heated. For a sequential evaporation of the analytes a defined temperature programme is applied. The vaporized sample is transported into the ICP by a carrier gas flow.[19] Laser ablation coupled to an ICP mass spectrometer will be discussed in further detail in chapter 2.3.

2.2.2 Plasma source

Inductively coupled plasma is the most common type of plasma source used today. It serves as a vaporization - atomization - excitation - ionization source for emission and mass spectrometry.[21]

The ICP is formed in a quartz torch, which consists of three concentric tubes surrounded by a load coil connected to a radio-frequency generator at the top end of the torch. Argon is typically used as gas supply.[22] A schematic illustration is shown in figure 2.3

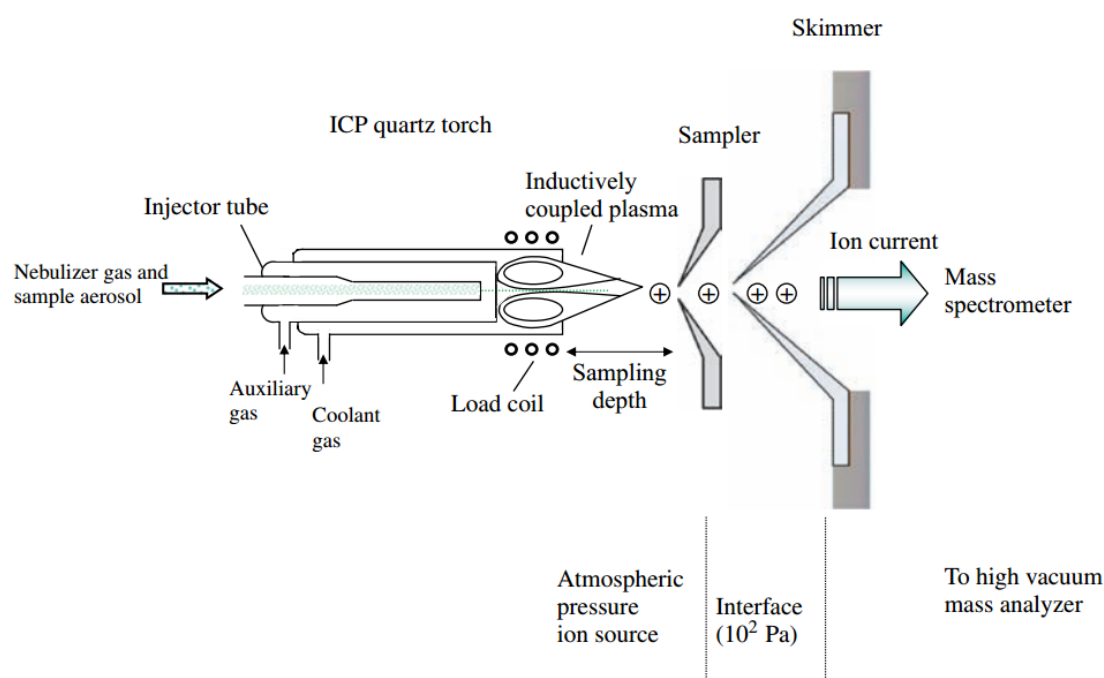


Figure 2.3: Schematic of an inductively coupled plasma source and interface region [19]

Via the inner tube, the sample aerosol together with the carrier gas is transported into the plasma. Commonly used nebulizer gas flow rates are $0.5 - 1.2 \text{ Lmin}^{-1}$. The two

outer tubes are used to transport the auxiliary gas ($0.8 - 1.2 \text{ Lmin}^{-1}$) and the cool gas ($10 - 20 \text{ Lmin}^{-1}$). [19] The cool gas, flowing through the outer tube, maintains the plasma and in addition cools the plasma confinement tube. The auxiliary gas, streaming through the middle tube, is needed to form and stabilize the plasma and in some cases push the hot ICP discharge away from the injector tube. In case of the Ar ICP either of the two outer gas flows will independently sustain a plasma. Therefore a sharp assignment of functions of the individual gas flows is not reasonable.

Applying radio-frequency power to the load coil produces an oscillating current inducing an oscillating magnetic field, which is necessary for igniting and sustaining a plasma. A high-voltage spark is used to initiate the plasma, causing ionization of the argon gas by collisions of argon atoms and electrons. Further electrons are released, accelerated through the magnetic field and are able to take part in the ionisation process. When the rate at which electrons are produced equals the rate at which they are consumed by recombination a steady-state plasma is obtained.

Typical plasma gas temperatures are between $5000 - 8000 \text{ K}$, depending on the RF power and the nebulizer gas flow rate. Moreover, the temperature of the ICP decreases with increasing distance from the load coil. Under these conditions, chemical compounds introduced into the plasma are atomized and ionized to a high degree. The ionization efficiency is a function of the ionization energy of the analyte. With increasing first ionization energy, the number of ionized analytes decreases. Although elements with an ionization potential of less than 8 eV are ionized with nearly 100% yield, only 1 in $10^4 - 10^6$ atoms in the original sample are detected due to transportation losses throughout the mass analyzer. [23] As an alternative to argon, mixed gas plasmas (e.g. Ar/He, Ar/N₂) have been used to limit the formation of polyatomic ions causing interferences in the mass spectrum. The application of helium plasmas enables the ionization of elements with high ionization energies. [21]

Not only analyte atoms are ionized, also polyatomic ions and doubly charged ions are formed due to recombination reactions, which takes place upon cooling. Polyatomic

ions are mostly attributed to the plasma/nebulizer gas used, matrix components in the sample/solvent or oxygen/nitrogen from air. Examples for the most prominent spectral interferences in an argon ICP are $^{40}\text{Ar}^+$, $^{40}\text{Ar}^{40}\text{Ar}^+$, $^{40}\text{Ar}^{16}\text{O}^+$, respectively $^{40}\text{Ar}^{12}\text{C}^+$ in organic samples or $^{40}\text{Ar}^{35}\text{Cl}^+$ in a hydrochloride acid medium. Different isotopes of one element might also create interferences at the same mass as the analyte. Possible ways to compensate for spectral interferences are the use of cool plasma technology, collision/reaction cells or high resolution mass analyzers particularly double-focusing sector mass analyzers.[24]

2.2.3 Interface region

The function of the interface region is to transport the ions formed in the plasma at atmospheric pressure to the high-vacuum mass analyzer. As shown in figure 2.3, the ion extraction interface consists of two metal cones usually made of nickel: the sampler and the skimmer cone. Both cones exhibit a small opening in the middle with a diameter of 0.8 - 1.2 mm for the sampler and 0.4 - 1.0 mm for the skimmer orifice. The transition from atmospheric pressure on the one side of the interface to high-vacuum on the other side is carried out by differential pumping, resulting in a pressure of approximately 130 Pa within the two cones. When expanding through the sampler cone, the plasma produces a gas jet whereat the central part of the jet passes through the skimmer orifice and is transported into the mass analyzer.[19]

The interface region is a very challenging component of ICP-MS instruments because the ions need to be transported efficiently, uniformly and with electrical integrity from the plasma to the mass analyzer [24]. An isolated Ar-ICP has a high RF potential, resulting from coupling of the voltage on the load coil and the plasma. This causes a secondary discharge between the plasma and the sampler cone inducing a series of negative effects: a very high continuum background, a reduced sampler lifetime, a wide ion kinetic energy distribution and an increasing number of doubly charged species. Originally the secondary discharge was avoided by grounding the load coil at the center thereby reducing the RF potential of the plasma to a few volts. In recent instruments elimination of the problem is achieved by a grounded conductive shield between the load coil and ICP torch, interlaced load coils or by balancing the circuit of the RF generator. [21]

2.2.4 Ion optics

In order to focus and direct the ions into the mass analyzer, ion optics in the form of electrostatically controlled lenses are located between the skimmer cone and the mass separation device. Consisting of a series of metal plates, barrel or cylinders each with a specific voltage, the ion beam is guided into the mass analyzer.

The ion trajectory after the skimmer cone is also influenced by the space-charge effect. Due to the mutual repulsion of ions within the ion beam, ions with lower mass are deflected more than ions with higher mass resulting in mass discrimination. Therefore analyte ions need to be directed back into the center of the ion beam by applying voltages on one or more lens components.

Secondly, the ion optics system is used to prevent particulates, neutral species and photons from reaching the detector. These species will lower the detection capabilities and increase signal instability. There are different approaches to overcome this problem: The mass analyzer is either positioned off-axis to the ion optics or the ion beam is deflected in a 90° angle that only positively charged ions are able to follow the course. Alternatively a metal disk is placed behind the skimmer cone, deflecting the ions while neutrals, photons and solid particles are stopped.[24]

2.2.5 Ion separation

The ion separation system is an essential part of the mass spectrometer and separates the ions formed in the plasma with respect to their mass-to-charge (m/z) ratio. In today's instruments, mass separation is achieved in a number of different ways depending on the separation system used. Sectorfield, Time-of-Flight (ToF) and quadrupole instruments are commercially available and will be explained subsequently in more detail.[24] A quadrupole mass analyzer has been used during present experiments.

Quadrupole technology

The majority of ICP-MS systems employ quadrupole mass filters as a result of their ease of use and low cost of manufacture. A quadrupole analyzer consists of four electrodes with a cylindrical or ideally a hyperbolic shaped profile as shown in figure 2.4.

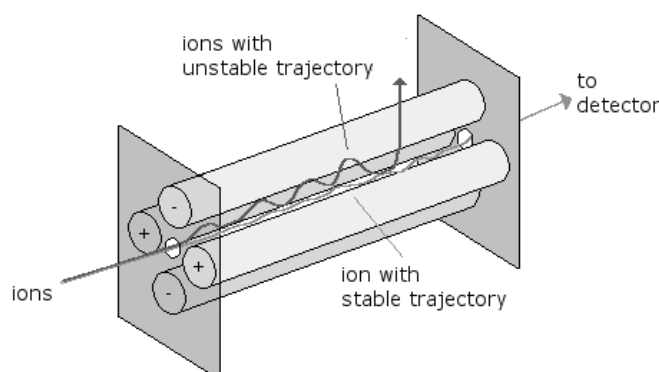


Figure 2.4: Schematic illustration of a quadrupole mass filter [25]

By applying a direct current (DC) and a time-dependent alternating current (RF) to opposite pairs of rods, a mass band-pass filter is produced. Meaning that only a narrow band of ion masses will pass the electrodes and reach the detection system. If V_0 is the amplitude of the RF voltage and U the DC offset, then V_0 determines the position of the band-pass and U/V_0 sets the width of the filter. The Mathieu equation describes the ion motion in a quadrupole. The solutions are complex and classified 'stable' and 'unstable'. Ions with an 'unstable' trajectory are filtered out because the amplitude of oscillation of the ions path increases exponentially until the ions strike a rod and are lost.

To let ions of different masses pass consecutively, the values of U and V_0 are varied while holding their ratio constant. [21]

Time-of-Flight technology

Time-of-Flight (ToF) systems allow simultaneous detection of the whole mass spectrum. The basic principle that they are based on is that the kinetic energy of an ion is directly proportional to its mass and velocity. In a ToF-instrument pulsed ion beams are accelerated into a field free drift tube whereby all ions exhibit the same kinetic energy. Each package consists of ions with different masses, hence different velocities. The analytes are separated in time over a fixed flight path distance. Lighter ions are faster than heavier ones. Therefore the lightest ions arrive first, followed by the medium ones. The last ones to reach the detector are the heaviest types. Ion beams are detected one after the other with increasing mass.[19]

In contrast to quadrupole or sector field technology, when using a ToF system the con-

tinuous ion beam generated in the plasma has to be “chopped” to provide ion packages at a frequency of a few kilohertz. The packets of extracted ions are then steered into the mass detector. This means, that only a fraction of the continuous analyte signal actually makes it into the analyzer. When considering a ToF-instrument this significant difference has to be kept in mind.[24]

Sector field technology

In a magnetic sector field mass spectrometer a homogeneous magnetic field is applied. The trajectory of an ion of mass m and velocity v flying into a constant magnetic field becomes a circular path with radius r_m . The radius depends on the mass of the ion, the strength of the magnetic field and the accelerating voltage, applied to adjust a certain kinetic energy.[25] Both focusing and dispersing of a monoenergetic ion beam occurs: due to the lens effect focusing for a divergent ion beam with the same mass occurs, because of the prism effect ions with different masses are dispersed. Using a single homogeneous magnetic field as a mass separation system is possible only if all the ions have similar energies. If ions of the same mass exhibit different kinetic energies, sharply focussing is not possible.

In addition, energy focussing has to be done by applying an electric sector field. The system consists of a cylindrical condenser with a positive voltage applied to the outer plate and a negative voltage applied to the inner plate. If an ion beam with ions of different masses and energies enters an electric sector field, the ions are deflected and fly on several paths. Ions of the same kinetic energy are focused. An electric sector field causes energy focusing only.

Magnetic and electric sector fields are combined in a double-focusing sector field instrument. Ions enter an electric and magnetic sector field usually in a forward or reverse Nier-Johnson geometry. In the forward design the electric sector field is positioned before the magnetic sector field, in the reverse design it is installed afterwards [24].

Ions entering the mass analyzer are deflected by a defined radius r_e of the electric sector field and r_m of the magnetic sector field. Therefore energy and directional focussing at a defined position is achieved, where the entrance slit to the detection system is installed. By varying the magnetic field, ions of various masses can be detected successively. The

big advantage of a double-focusing sector field analyzer is the high mass resolution, allowing the analysis of elements that are susceptible to plasma gas-, solvent- or sample-based spectral interferences.[19]

2.2.6 Detection

The detection system, positioned after the mass analyzer converts the ions into an electrical signal which is then processed by an integrated measurement circuitry. Ion counting systems are usually used for low signal ranges while some kind of analogue measurement is employed for higher signals.[21]

In an ion counting system, called electron multiplier, ions are directed onto a dynode at high voltage. By the impinging of the ions, electrons are released, accelerated and then directed onto another dynode. The dynodes are connected to increasing positive potentials. A large number of electrons will be generated after sufficient repetitions leading to a gain of $10^6 - 10^8$. At the end, the electrons are directed to a collector electrode, causing a pulsed signal. Individual electron pulses are detected via pulse counting electronics.[19][21]

Analogue collection is achieved by reducing the voltage applied to the electron multiplier. Operated in this mode, the resulting current at the collector electrode can be measured in an analogue mode. The typical gain is between $10^3 - 10^5$. [21]

By combining the two operation modes an extension of the dynamic range is possible. The detector operates in the pulse mode for low ion currents and in analogue mode for high ion currents.[19]

2.3 Laser ablation coupled to an ICP-MS

Laser ablation is a highly-accepted method for the direct analysis of solid samples and allows examination of various materials ranging from conductive and non-conductive inorganic and organic compounds. Determination of major, minor and trace elements as well as spatially resolved studies are possible.

Using laser ablation, none or relatively simple sample preparation is required. No chemical procedure for dissolution is necessary, reducing the risk of contamination or

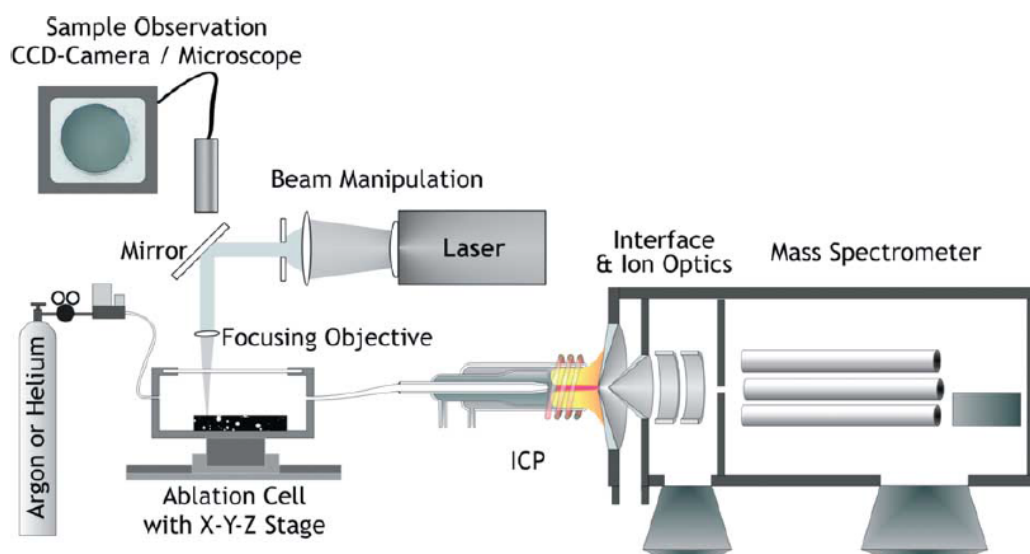


Figure 2.5: Schematic set-up of LA-ICP-MS [27]

sample loss and shorten the overall sample preparation time. In combination with ICP-MS, LA offers high sensitivity, a wide dynamic range and relatively simple spectra. Moreover, sampling and excitation/detection can be optimized separately.[26][27][28][29]

During laser ablation the sample is put in an ablation system where a laser beam is focused onto the sample surface as shown in figure 2.5. Material will be ablated if the energy density is sufficiently high. The generated aerosol consists of sample vapor, particles and agglomerates and is transported into the plasma via a carrier gas stream. The plasma serves as a separate excitation source where positive ions are formed. Subsequently the ions are extracted and analyzed in a mass spectrometer.[27]

When laser light interacts with the sample, the electromagnetic laser radiation is able to directly break the atomic lattice if the photon energy is higher than the bonding energy of the solid. Electrons may also absorb the laser light why melting and vaporization of the target material occurs. In addition, a plasma plume is generated in the early stage of the ablation process, which also leads to a removal of the target material. Various operating parameters like laser wavelength and pulse duration as well as the gas environment used for aerosol transportation influence the composition and particle-size of the aerosol formed.[26] [27][28]

However, laser ablation exhibits non-stoichiometric effects called elemental fractionation which has been observed during ablation of different homogeneous samples. Elemental fractionation occurs during sampling, aerosol transportation and within the plasma. It is caused by the different thermal behaviour of elements present in the sample and the resulting particle sizes of the sample aerosol. If a wide particle-size distribution is obtained, atomization and ionization in the ICP may not be achieved for larger particles. For example, the formation of micrometer-sized particles produced from nanosecond Nd:YAG lasers strongly affects precision and accuracy because evaporation and ionization turned out to be insufficient in the ICP. The efficiency of vaporization of elements in larger particles depends on the vaporization index. Volatile elements exhibit a higher degree of atomization in comparison to refractory elements, indicated by a lower vaporization index. To generate particle-sizes that can be fully atomized in the ICP and therefore reduce elemental fractionation appropriate laser operating conditions have to be found. Elemental fractionation is a matrix-dependent phenomenon, meaning that without matrix-matched standards quantitative analysis is limited.[30][31][32]

2.3.1 Instrumentation

A laser ablation system consists of a high-power laser, beam steering and focusing optics, an ablation chamber and interface connections to the detection systems, like ICP-MS.[21]

Different laser systems are available today, mostly using Nd:YAG or excimer lasers. The ablation behaviour is mostly influenced by the laser wavelength and pulse duration.[33] The fundamental wavelength of a Nd:YAG laser is in the near IR at 1064 nm. Today's dominant UV-wavelength 266 nm and 213 nm have been achieved through optical frequency quadrupling and quintupling. When using an excimer laser, the output wavelength is determined by the operating gas (e.g. 193 nm for ArF). The shorter the wavelength, the higher the provided photon energy resulting in a larger ablation rate and less fractionation which means that the ablation of the sample material is independent of the thermal behaviour of the included elements. [26] In addition, when using shorter pulse widths less fractionation has been observed due to less thermal diffusion in the material. A trend

towards shorter wavelengths and pulse duration is observable today.[30][34] Apertures are used to homogenize laser-beam profiles ensuring an 'even' energy profile through the ablation spot.[27] Also focusing to small spot sizes, allowing spatial resolution down to 2 - 5 μm , is possible.[21]

During ablation, the sample is put in an airtight ablation chamber placed on an XYZ translational stage, allowing the positioning of the sample. Positioning and focusing is possible via a CCD camera. Various designs of ablation cells have been created, mostly varying in internal volume. The ablation chamber is flushed with an inert gas, usually He to transport the sample aerosol via transfer tubings into the plasma. If the transfer path is too complex analyte deposition may occur.

Important characteristics of a given ablation cell are a high transport efficiency and a low memory effect. Transport efficiency is measured as signal intensity and does not change significantly for different volumes of ablation cell and tubing. Transport efficiencies of > 70 - 90 % are achieved today. The volume of the ablation chamber and transport path influence the signal dispersion determining the signal/background ratio.[27][30] Smaller volumes and a high carrier gas flow rate may also decrease sample washout time and memory effects [26].

2.3.2 Operating parameters

The operating conditions strongly depend on the analytical problem and the type of sample present. In addition, operating conditions of the ICP, laser characteristics and ablation cell design effect signal response as mentioned previously.

Important characteristics like power output, wavelength, repetition rate, shot-to-shot reproducibility, thermal stability and ease of alignment and operation must be considered when choosing a laser. The amount of laser energy controls the ablation yield and the resulting signal response. In general, increasing the laser output energy produces an increased signal response. A minimum amount of energy, the ablation threshold has to be present to ablate any material.[21] During laser ablation surface heating and melting, ejection of material and the formation of craters occurs. The proportion of ablated material present as vapor, molten droplets and solid particles strongly depends on laser power,

power densities and the associated temperatures. Producing a fine aerosol with a narrow particle size distribution is favourable[35]. When working with high energy densities, a laser-induced plume is formed above the sample surface, absorbing penetrating laser light and resulting in secondary ablation. Shorter laser wavelengths and pulse duration result in less fractionation as mentioned in chapter 2.3.1. [35][22]

The laser focus is one of the few parameters set manually. Because the focus point changes during ablation energy transfer to the sample surface is affected. Defocusing may influence sensitivity for several sample matrices.

Finally, representative sampling is crucial. The laser beam may continuously strike on a single spot or the sample moves under successive laser shots. A single shot produces a transient signal, firing at a sufficiently high repetition rate results in a continuous signal. [21] Quadrupole-based systems are mostly used allowing very fast scanning over the mass spectrum. ToF-instruments permit simultaneous sampling but current instruments exhibit inadequate sensitivity for nonrestrictive trace and ultratrace analysis.[27][36]

2.4 Scanning electron microscopy (SEM)

A scanning electron microscope scans a focused electron beam over a sample surface to produce an image. The primary electrons in the beam interact with the atoms in the specimen in various ways. The produced signals are used to obtain an image containing information about the surface topography and composition.

Scanning electron microscopy offers high resolution and magnification, whereat the resolution is limited by the diameter of the electron beam. The smaller the diameter, the better two adjacent surface structures are optically distinguishable. The minimal possible beam diameter in conventional SEMs is a few nanometers. Other advantages are a high depth of focus and simple sample preparation.

SEM is used for numerous samples in biology, medicine and materials science. Investigated materials must be resistant to vacuum and electrically conductive. Non conductive samples are examined after application of a thin, conductive metal film on the surface.[37][38]

2.4.1 Instrumentation

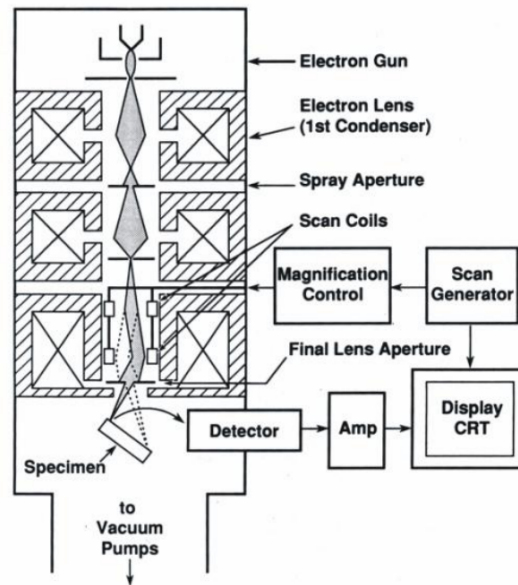


Figure 2.6: Schematic set-up of a SEM [39]

A schematic illustration of a scanning electron microscope is shown in figure 2.6. Electrons are generated in an electron gun, consisting of a cathode, a Wehnelt cup and an anode. The cathode serves as the electron source. Basically there are two types of electron guns: thermionic and field emission.[40]

In a thermionic electron gun, electrons are emitted from a tungsten or lanthanum hexaboride (LaB_6) filament. Tungsten cathodes are prepared as a wire bent into a hairpin and are heated by applying a voltage between the two ends of the wire. The life-time of a tungsten cathode is limited to approximately 220 h due to evaporation of the cathode material. However, tungsten cathodes are relatively cheap and a simple vacuum system is sufficient to keep the cathode from oxidation. Cathodes prepared from a LaB_6 monocrystal are operated in a similar way as tungsten cathodes offering several advantages over the latter: extended lifetime and higher brightness meaning higher resolution. Disadvantages are elevated costs and the requirement of a better vacuum.[40][37]

A field emission electron gun works by applying a strong electric field to a tungsten tip, enabling the emission of electrons by the wave-mechanical tunnelling effect. The

generation of electrons is possible without the application of thermic energy. Field emission cathodes offer even higher brightness and longer lifetime, though the system is more expensive and complex and ultra high vacuum is required. [40]

The emerging electrons are then accelerated towards the anode. The potential difference between the cathode and anode determines the energy and wavelength of the electron. Typical acceleration voltages are between 1 - 30 kV. The electron gun of some thermionic devices is encircled by a metal capsule, called Wehnelt cylinder. It has the function of an electrostatic lens, focussing the electrons in front of the anode.

After passing the anode, the electron beam is focused by an electron lens system. Two or three magnetic lenses are used to demagnify the directed beam from the Wehnelt cylinder. The goal is to minimize the beam diameter as much as possible. Electron lenses consist of a current-carrying coil with a ferromagnetic core generating a magnetic field. The condenser lenses are used to regulate the beam current by adjusting the beam diameter. The objective lens focuses the electrons onto the sample.[37]

Finally, an image is generated by scanning the electron beam in a raster pattern over the sample surface. The primary electrons interact with the specimen, generating electrons, characteristic radiation, light and so on (detailed information see chapter 2.4.2). The emerging electrons are either detected with a scintillator crystal or with a scintillator or semiconductor device, depending on their kinetic energy. For the measurement of characteristic X-ray radiation, energy-dispersive and wavelength-dispersive spectrometers are used.[37][41]

2.4.2 Electron-sample interactions

Elastic and inelastic scattering are the elementary interaction processes when electrons impinge on the surface of a solid-state material. Elastic interactions occur between the electron beam and the atomic nucleus leading to a deflection of the electron. Inelastic processes happen between the electrons and the electrons of the electronic shell of the sample, causing excitation of electronic states.

Elastic and inelastic scattering therefore cause a lateral broadening of the finely focused

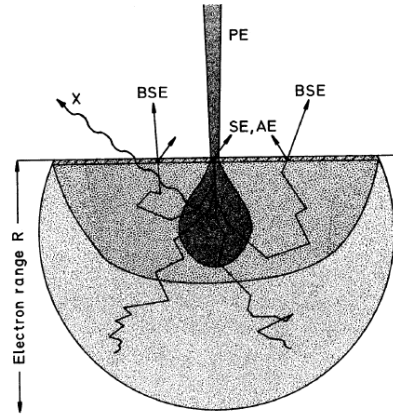


Figure 2.7: Information depth of secondary electrons (SE), backscattered electrons (BSE), Auger electrons (AE) and characteristic radiation (X).[40]

electron beam. Electron trajectories spread into the bulk of the material, depending on electron energy and target density. However, the information volume that contributes to each of the possible signals depends on where the corresponding interaction takes place. Figure 2.7 shows the most important signals generated and their information volume.[40][41]

Elastic interactions

In an elastic process, energy and momentum are conserved resulting in a high kinetic energy of the backscattered electron (BSE). Scattering of primary electrons occurs due to the Coulomb interactions with the atomic nuclei. Furthermore, an electron must be deflected by at least 90° to be detected. Mostly multiple small-angle scattering events take place, but also large-angle scattering is possible. To which extent backscattered electrons are produced strongly depends on the atomic number of the sample. Hence differences in the atomic number can be visualized in a BSE picture. [41][37]

Inelastic interactions

The most important inelastic interactions in SEM are those where secondary electrons (SE) are produced. Part of the kinetic energy of the impinging electron is transferred when the electron beam and the atomic shell interact. Consequently, secondary electrons exhibit low kinetic energy.

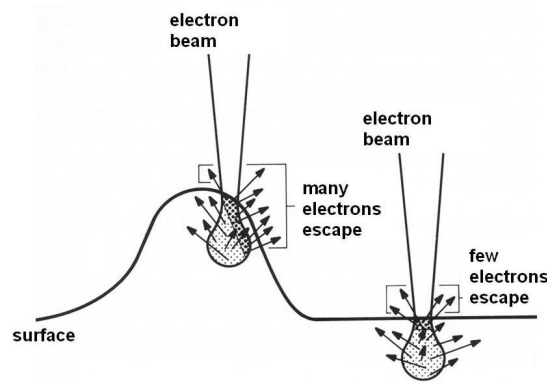


Figure 2.8: Image creation using secondary electrons (SE)[37]

SE are generated by ionization of electronic levels during primary electron impact. These electrons are generated in the entire information volume, but due to their low energy a large portion gets absorbed by the sample. Only secondary electrons produced nearby the sample surface are able to leave the specimen. Figure 2.8 shows the principle of absorption and exit of electrons crucial for image creation. Simply electrons generated in the darker portion of the excitation plume are able to leave the sample. Thus, more secondary electrons are able to exit on a small elevation of the surface, making this region brighter in the generated image. As a result, secondary electrons are essential for topographical imaging. Pictures created from SE show the highest resolution and a high depth of field.[37]

Further ionization of inner orbitals might take place due to inelastic scattering. To compensate the imbalance, an electron is transferred from an upper to a lower level. As a result, characteristic radiation and Auger electrons are generated. The energy of the emitted X-ray photon is equivalent to the difference in binding energies and can be measured to identify the source atom.[41]

Alternatively to the emission of characteristic radiation, an Auger electron may be produced. The energy that is released when an electron from an outer shell fills the vacancy in the ionized shell is transferred to another atomic electron which is able to leave the sample. Similarly to secondary electrons, Auger electrons are able to exit the specimen only from a thin layer of the surface.[40]

3 Experimental

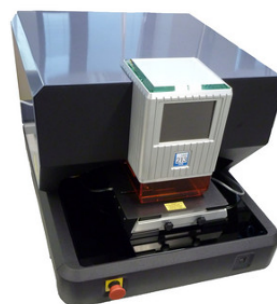
3.1 Instrumentation

Experiments were performed using a quadrupole ICP-MS (iCAP Q, Thermo Scientific) as shown in figure 3.1 (a). Data acquisition was done by the Qtegra software (v 2.4.1800.192) provided with the instrument.

A commercially available Nd:YAG nanosecond laser ablation system (NWR213, ESI), illustrated in figure 3.1 (b) with a fast-washout-cell was coupled to the ICP-MS for solid sampling. The aerosol was transferred via PTFE tubings. Helium was used as ablation gas and mixed with Argon through a Y piece in the transfer line.



(a) iCAP Q, Thermo Scientific [42]



(b) NWR213 Laser Ablation System, ESI [43]

Figure 3.1: Equipment used for performed experiments

The instrument parameters were optimized before every experiment, using a reference material (NIST SRM 612, National Institute of Standards and Technology). The ICP-MS was tuned for maximum ^{115}In signal intensity while ablating the solid standard. The

measurements were carried out using the laser parameters listed in table 3.1. ICP-MS settings are given in table 3.2.

Laser parameters	Standard	Pre-ablation	Sample measurement
Fluence [J cm^{-1}]	-	3 - 4	4 - 17
Beam diameter [μm]	80	80 - 150	3 - 10
Repetition rate [Hz]	10	2 (5 sec)	5 - 20
Output [%]	70	40 - 50	40 - 70
Scan speed [$\mu\text{m sec}^{-1}$]	5	-	2 - 5
Carrier gas flow [L min^{-1}]	0.75	0.75	0.75

Table 3.1: Laser ablation system measurement parameters

ICP-MS parameters	
RF power [W]	1550
Nebulizer gas flow rate [L min^{-1}]	0.8
Plasma gas flow rate [L min^{-1}]	12
Auxiliary gas flow rate [L min^{-1}]	0.8
Dwell time [ms]	0.01
Cones	Ni

Table 3.2: ICP-MS measurement parameters

Additional analysis of the samples was done using optical microscopy (DM2500M, Leica) and scanning electron microscopy (Quanta 200, FEI) equipped with an energy dispersive spectrometer (EDX). Optical microscopy was used to verify sample preparation techniques, whereas SEM was used to validate obtained elemental distribution from laser ablation experiments.

3.2 Sample characterization

The samples were provided by the institute for water quality, resource and waste management (E226, TU Vienna). Two different types of fly ash, collected from contrasting sectors of industry, were analyzed:

FLA - collected from a municipal waste incinerator in Spittelau, Vienna

HZ9 - collected from a blast furnace at voestalpine AG, Linz

The particle size distribution of the powdered samples was analyzed using a Mastersizer 2000 (Malvern instruments Ltd). HZ9 showed a bimodal distribution profile with maxima between 50 - 80 μm and 1 - 5 μm . The latter were insignificant for the following experiments. The FLA fly ash sample revealed a unimodal distribution profile with a maximum between 50 - 70 μm particle size.

3.3 Sample preparation

The aim of sample preparation was to capture single, isolated fly ash particles of all particle sizes and preventing them from breaking loose during laser ablation or vacuum application. To do that, several single steps had to be introduced and optimized. First of all, a method for the dispersion of particles had to be ascertained. Then suitable mounting media and sample carriers as well as a technique for particle fixation were tested. In the end, a procedure to examine captured particle sizes and particle distribution had to be found.

3.3.1 Particle dispersion

A self-combined device was developed to dispense the fly ash samples. A schematic illustration is shown in figure 3.2. The apparatus consists of a standard ICP-OES cyclonic spray chamber and a custom made glass elbow piece. First, 10 mg of sample were weighed in the spray chamber. Afterwards, an applied Argon stream (0.5 bar, adjusted pressure at the line-mounted valve) transferred the sample onto a prepared mounting media.

3.3.2 Deposition strategy

Tops and/or bottoms of petri dishes were designated as basis for particle deposition. First, the petri dish surface was coated with a thin gold layer with a sputter coater (B7340, Agar Scientific). The sample cell was evacuated to a pressure of approximately 0.1 mbar.

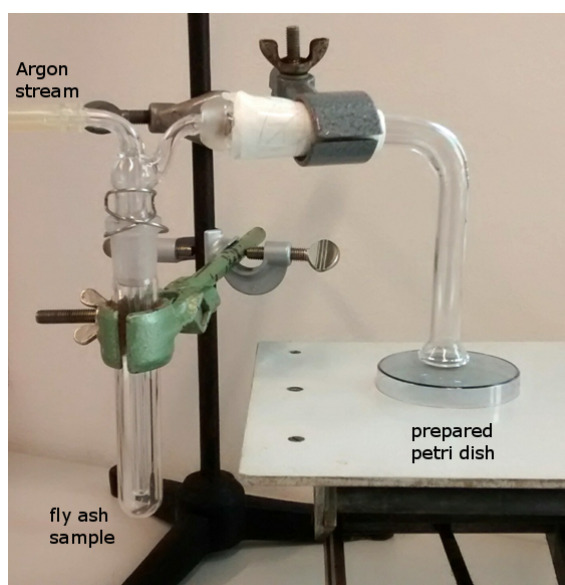


Figure 3.2: Device for sample dispersal

Then coating was done for 40 sec with a distance of 4 cm from the sputtering source and a current of 10 mA. Afterwards, anti-static spray (Antistatik 100, Kontakt Chemie) was applied and dried at room temperature. In contrast to other fixation media, e.g. hairspray, tape, epoxy resin which were tested before, anti-static spray offered enough adhesive strength but prevented particles from overlapping. Then the prepared petri-dish was placed under the dispersion device.

After fly ash application, hairspray (3 Wetter taft, Schwarzkopf) was used to fixate the particles. An overview of all applied layers is shown in 3.3.

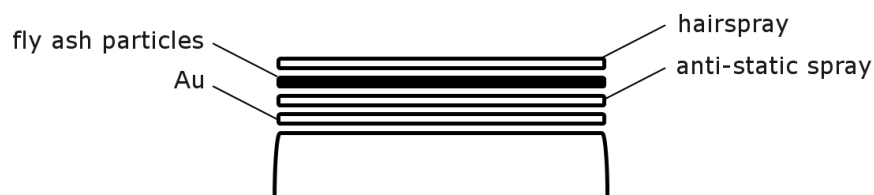


Figure 3.3: Schematic illustration of sample preparation

3.3.3 Verification strategy

The so-prepared samples were analyzed with optical microscopy and ImageJ software (1.46r, Wayne Rasband, National Institutes of Health, USA) to verify that different particle

sizes were present and consistent with the measured particle size distributions.

Approved samples were named according to the following schematic:

(xx)_sample_pressure_sticky surface

xx - continuing numbering

sample - FLA or HZ9

pressure - adjusted pressure at the line-mounted valve

sticky surface - A...anti-static spray, H...hairspray, K...adhesive tape

3.4 Laser ablation experiments

For laser ablation experiments whole petri dishes were put in the ablation chamber. Then the chamber and the gas lines were purged with He carrier gas (0.5 L min^{-1}) for at least 15 min before ablation.

3.4.1 Preparation of cross-section areas

In general, particles with diameters between $60 - 120 \mu\text{m}$ were selected for analysis. A schematic of the measurement procedure is shown in figure 3.4. First, single particles were ablated with a beam diameter larger than the particle diameter to obtain a cross section. Due to different shapes, orientation and composition, it was impossible to locate the center of a particle during pre-ablation. But, different core-shell composition should be detectable at any cross-section. Only the thickness of the shell might change. Optimized parameters for pre-ablation are shown in table 3.1. The beam diameter and the laser energy were adjusted to reach a fluence of $3 - 4 \text{ J cm}^{-1}$ for every particle. Ten shots per piece turned out to be sufficient for large and smaller ones.

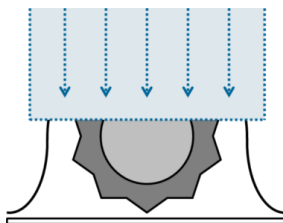


Figure 3.4: Schematic illustration of the pre-ablation procedure

3.4.2 Linescan measurements and operating conditions

Linescan measurements were conducted to analyze sample composition over a particles cross section. The aim was to find out if core and shell of a particle show different element distribution in an easy and fast way. The laser energy and the beam diameter were optimized to reach sufficient ablation of material for analyte detection on the one hand, and the highest possible resolution on the other hand. Before any other experiments, a survey scan was conducted to determine the elements present in both fly ash samples.

Subsequently, a linescan pattern was drawn on the previously prepared cross-section as shown in figure 3.5. Optimized laser parameters and measured isotopes are shown in table 3.3. Because the petri dish surface has been coated with a thin Au layer during sample preparation, isotope ^{197}Au was used to differentiate between particle and background while scanning with the laser.

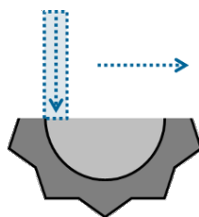


Figure 3.5: Schematic illustration of a linescan measurement

	FLA	HZ9
Main Analytes	^{27}Al , ^{48}Ti , ^{66}Zn , ^{197}Au , ^{208}Pb	^{27}Al , ^{197}Au , ^{208}Pb
Laser parameter	50 %, 10 Hz, 5 μm , 2 $\mu\text{m sec}^{-1}$	
Fluence	5 - 6 J cm^{-1}	
Secondary Analytes	^{55}Mn , ^{63}Cu , ^{120}Sn , ^{121}Sb , ^{197}Au	^{48}Ti , ^{55}Mn , ^{66}Zn , ^{120}Sn , ^{197}Au
Laser parameter	50 %, 10 Hz, 10 μm , 2 $\mu\text{m sec}^{-1}$	
Fluence	5 - 6 J cm^{-1}	

Table 3.3: Laser parameters for linescan measurements

3.4.3 Image creation and optimization

To receive more detailed and most importantly space-resolved information about elemental distribution, imaging experiments were conducted. Based on the previously performed linescan measurements, information on laser parameters and analytes was obtained.

Image measurements

A laser beam with either 3 or 5 μm and a scan speed of 3 $\mu\text{m sec}^{-1}$ was used throughout all imaging experiments. Mapping was done creating a single linescan pattern with the desired laser adjustments. Then the linescan was multiplied to create a rectangular linescan pattern over the particles cross-section, as shown in figure 3.6. During the measurement, the scan direction was from the left side of the particle to the right side for every line. This means that the laser fired from left to right, stopped at the end of each line, moved back to the left edge of the pattern and started again. This approach led to defined interruptions of the recorded analyte signals, also for the background signal ^{197}Au which was necessary for automatic image creation.

The complete set of laser parameters and measured isotopes is listed in table 3.4.

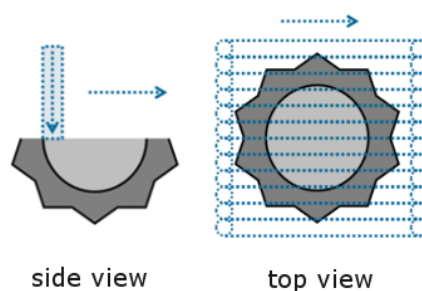


Figure 3.6: Schematic illustration of an image measurement

	FLA	HZ9
Analytes	^{27}Al , ^{48}Ti , ^{66}Zn , ^{197}Au , ^{208}Pb	^{27}Al , ^{197}Au , ^{208}Pb
Laser parameter	50 %, 20 Hz, 5 μm , 3 $\mu\text{m sec}^{-1}$ / 80 %, 20 Hz, 3 μm , 2 $\mu\text{m sec}^{-1}$	
Fluence	6 - 7 / 18 - 19 J cm^{-1}	

Table 3.4: Laser parameters for imaging with LA-ICP-MS

Digital image creation

The signal intensity of the traced isotopes was recorded by the Qtegra software and exported as a *.csv* file after measurements were performed. Image creation was done as suggested by Bonta et al [44] using ImageLab Software (v 1.02, Epina GmbH). During the import of the *.csv* files, an ever-present analyte signal had to be assigned (^{197}Au) as well as scan direction and measurement mode. The resolution was set automatically: the vertical number of pixels resulted from the number of detected lines, the horizontal number of pixels was set to the same number but could be changed manually. Then, the elemental image was created. Various adaptations were possible to perform, like attachment of a SEM image, correction to an internal standard etc.

3.5 Method validation using SEM-EDX

To verify images generated from laser ablation, SEM and EDX analysis of prepared particle cross sections was performed. Therefore particles were marked with a clearly visible laser pattern after pre-ablation. With the aid of the laser-labelling, the particles were recovered in the electron microscope. To prevent charging, additional sputtering with Au was done prior to the SEM analysis. The sputter coater parameters were adopted from sample preparation.

SEM investigations were conducted under high-vacuum conditions with an operating distance of approximately 10 mm. The accelerating voltage was set to 10 kV. Other instrument parameters were set by the operator.

Imaging using laser ablation was done subsequently.

4 Results and Discussion

4.1 Sample preparation

The aim of sample preparation was to apply single particles of all sizes and to retain them during laser ablation or vacuum conditions in SEM. The capture of isolated particles was crucial because imaging experiments were only reasonable without the occurrence of interferences from overlapping particles or agglomerates. Additionally, representative application of all present particle sizes was necessary to allow complete sample characterisation. For this purpose, it was essential to ensure that the obtained particle size distribution on the sample carrier corresponded to the particle size distribution of the real fly ash powder. Only if this condition was met, it would be possible to analyze all relevant particle sizes and to determine differences between single size ranges. Furthermore, a parameter to differentiate between sample and mounting base had to be found. In this case ^{197}Au was used and sputtered on top of the petri dishes prior to sample application.

During sample preparation, fly ash particles were put on a specially prepared sample carrier for further analysis using different mounting media and application styles. Among the mounting media tested were anti-static spray, hairspray and tape. The sample was applied either manually or with a self-constructed device as shown in figure 3.2 (chapter 3.3). Here, the Argon stream was adjusted with a line-mounted valve, set to pressures up to 2 bar.

An overview of the tested attachment layers and application conditions is given in table 4.1. In the end, using anti-static spray as mounting medium and the self-constructed device with a pressure ≤ 0.5 bar for sample application turned out to provide the best sample preparation strategy.

mounting media	application style
anti-static spray	manually
hairspray	application device with ≤ 0.5 bar
tape	application device with >0.5 bar

Table 4.1: Experimental parameters for sample preparation

For comparison, figure 4.1 shows all tested mounting bases with fly ash deposited in the optimized application way. It has been found out that manual deposition was inadequate for all surfaces as aggregation of particles occurred. Therefore, application using the already discussed device was preferred. Depending on the mounting medium, different experimental parameters were adjusted.

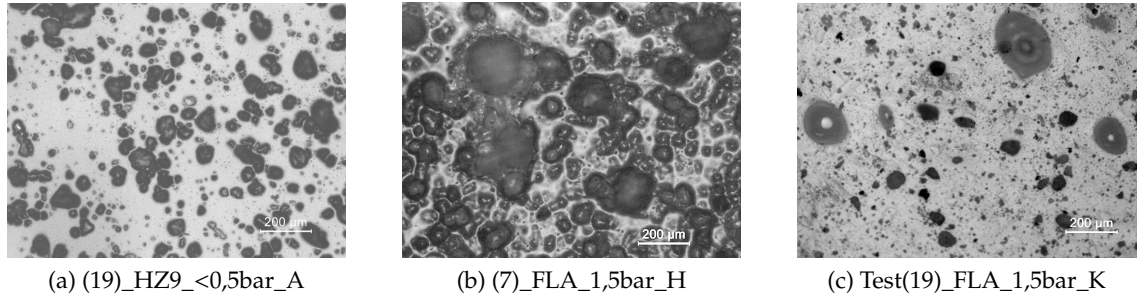


Figure 4.1: Comparison of different mounting media
(a) anti-static spray , (b) hairspray (c) tape

When using anti-static spray as a base, illustrated in 4.1 (a), pressure was set to the lowest possible value, at least not more than 0.5 bar at the line-mounted valve. A good separation, also in the densely coated area of the petri dish was received. Some aggregation and overlapping occurred, but also a lot of single, isolated particles were visible. Particle sizes ranged from a few μm up to over 100 μm for both, FLA and HZ9. Obtained particle size distribution will be discussed later on in this chapter in greater detail.

Figure 4.1 (b) shows a sampled petri dish with hairspray used as the attachment layer. As it can be seen, particle deposition is more dense compared to the anti-static spray sample. Nevertheless, when comparing the overall usability, a great number of particles suited for measurement were found using either anti-static spray or hairspray. A mild drawback of the latter is the slightly more delicate sample preparation procedure because the hairspray needed some time to dry after coating of the petri dish. The length of drying

time affected the amount and size of fly ash particles retained on the surface. Hence, another variable had to be optimized during method development. The optimized drying time was set to 2.5 min. The applied pressure at the valve was 1.5 bar whereas different values did only slightly affect particle distribution and retained sizes.

Tape as mounting media, see figure 4.1 (c) was discarded after only a few experiments. Although particle distribution seemed satisfactory, the surface of the tape itself was too rough especially for optical microscope analysis.

When using the self-constructed application device for sample preparation, no completely uniform distribution of particles was achieved. A schematic of a prepared petri dish surface is displayed in figure 4.2 (b). This particle distribution was obtained independent of the type of mounting media and was due to the installation of the application device and the placement of the petri dish. The illustration shows a densely coated area in the middle in the shape of a circle. An example of an associated particle distribution received from there is given in figure 4.2 (a). As it can be seen, particles of different sizes were present. Some agglomerates were visible too, but individual particles were accessible. Still a lot, but lesser particles covered the rest of the surface as shown in figure 4.2 (c). Particles in this area tended to be slightly smaller than in the middle area. On the other hand, the discovery of isolated particles was easier. The grey area in the image shows the sphere where most suitable particles were located.

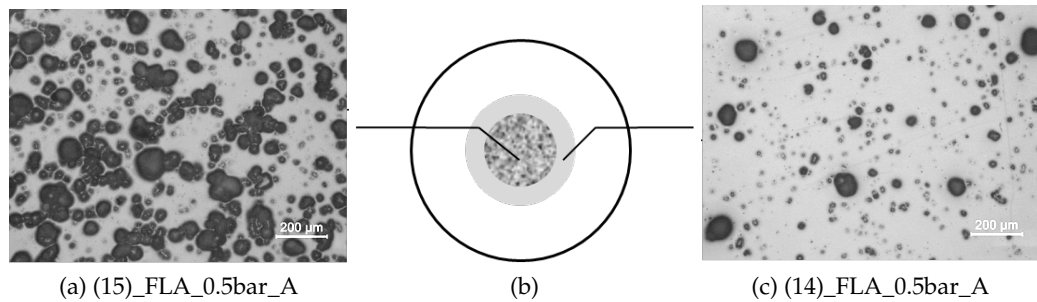


Figure 4.2: Particle distribution obtained on the surface of a petri dish
 (a) particle arrangement in the densely coated area in the middle of the sample carrier, (b) schematic of the appearance of a sampled petri dish surface, (c) particle arrangement outside the densely coated area in the middle of the sample carrier

As a final sample preparation step, particle size distribution of selected petri dishes was analyzed with ImageJ software and compared to the measured particle size distribution obtained from a Mastersizer 2000. In the example shown subsequently, pictures of the diameter of a sampled petri dish were taken using optical microscopy. Ten pictures were merged respectively, due to memory issues. Afterwards, merged pictures were loaded into ImageJ and converted to binary. The scale was set using the scale bar from optical microscopy. Then the Feret's diameter, which is the longest distance between any two points along the selection boundary was evaluated. In this context, particles with circularity of less than 0.4 or a diameter less than $50\text{ }\mu\text{m}$ were discarded.

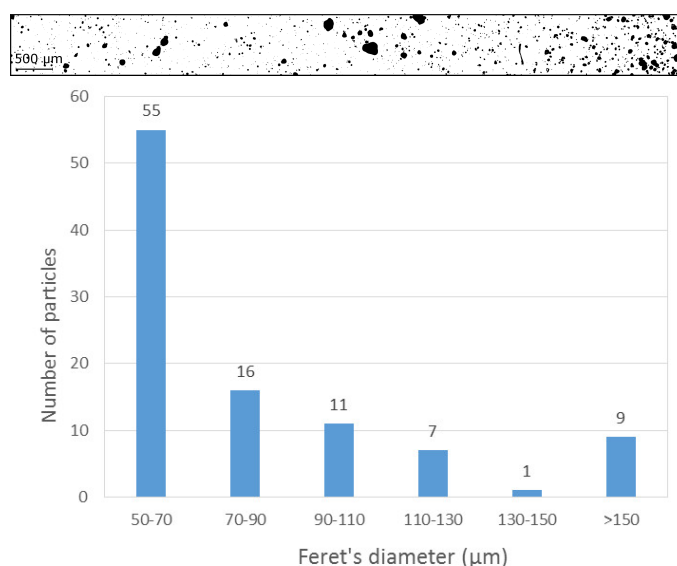


Figure 4.3: Particle size distribution of a section of (19)_HZ9_<0,5bar_A

Figure 4.3 shows the selected surface area of sample (19)_HZ9_<0,5bar_A converted to a binary picture with ImageJ. In addition, the associated particle size distribution is shown. Although more than 500 of them were counted, particles with a Feret diameter $< 50\text{ }\mu\text{m}$ were neglected because they were too small for LA-ICP-MS analysis. This high number resulted from the fact that smaller/lighter particles were more easily attached to the mounting medium. Additionally, a disruption of particles might have occurred during application. The automatic image evaluation may also lead to increased values. Despite that, sufficient particles with sizes $> 50\text{ }\mu\text{m}$ were captured.

Subsequently, individual petri dishes were analyzed taking a microscope picture of a

single spot suitable for laser measurements. Independent of the position on the petri dish similar particle size distributions were obtained.

4.2 Realization and optimization of pre-ablation

In order to analyze elemental distribution, a cross-section of a single particle had to be obtained as a first step. Ideally, one third to a half of the particle ought to be removed by laser ablation. However, locating the center of the particle during laser firing turned out to be impossible due to different shapes, orientation and composition of the fly ash. As different composition of core and shell should be detectable at any cross-section, independent of the mass removed, the executed strategy was to shoot at a particle with mild conditions and a low repetition rate.

A second challenge was that the inner structure of a particle was unknown, only the surface was observable using optical microscopy or SEM (secondary electron microscopy). A potential alteration of the fly ash during pre-ablation would therefore not have been determinable. As a result, applying mild laser conditions with low fluence values was preferred to keep the impact from pre-ablation as low as possible. Additionally, during subsequently performed linescan or imaging experiments an ablation of several μm takes place. Even if the cross-sections' surface was altered during pre-ablation, the obtained signal response from the linescan measurement would mainly contain signal from lower lying, untreated areas resulting in reliable measurement data.

Moreover, the laser diameter was set larger than the particle diameter to remove hairspray from the surrounding area. This allowed adequate ablation of the gold base coating to distinguish between the particle and the background signal.

The selection of appropriate laser conditions was done by observing the fly ash sample during pre-ablation with the CCD camera installed in the laser unit. An example is given in figure 4.4. The original size of the displayed particle was approximately $60\ \mu\text{m}$. The figure shows the alteration of the selected spot after 10, 20, and 30 laser shots with an optimized fluence of $3\text{--}4\ \text{J cm}^{-1}$. Obviously, the particle shrank with advanced laser treatment. The aim during the optimization of pre-ablation was to determine the amount of laser shots necessary to prevent particle shrinkage but enable sufficient mass removal

to obtain a cross-section. In this case, 10 to 20 shots were set as the threshold limit. The obtained number of shots was mainly dependent on the sample composition e.g. soot, iron or CaO as main component. The particle size, on the other hand, only had a small influence.

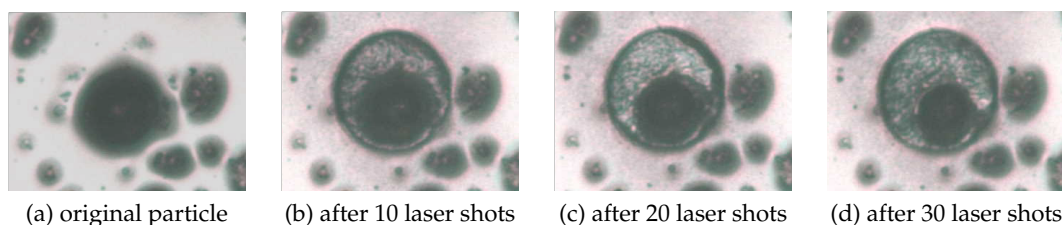


Figure 4.4: Transformation of a FLA fly ash particle during pre-ablation

To receive standardized laser settings, different particle sizes of FLA and HZ9 were analyzed. Ten shots with a fluence of $3-4 \text{ J cm}^{-1}$ per particle turned out to be sufficient for particle ablation and hairspray elimination. For further experiments, particles were classified into size categories and diameter and laser power were adjusted accordingly. Exemplary laser parameters are given in table 4.2.

Particle diameter [μm]	Laser diameter [μm]	Laser power [%]
< 80	125	45
80 - 100	150	50
100 - 125	175	60

Table 4.2: Experimental parameters for pre-ablation

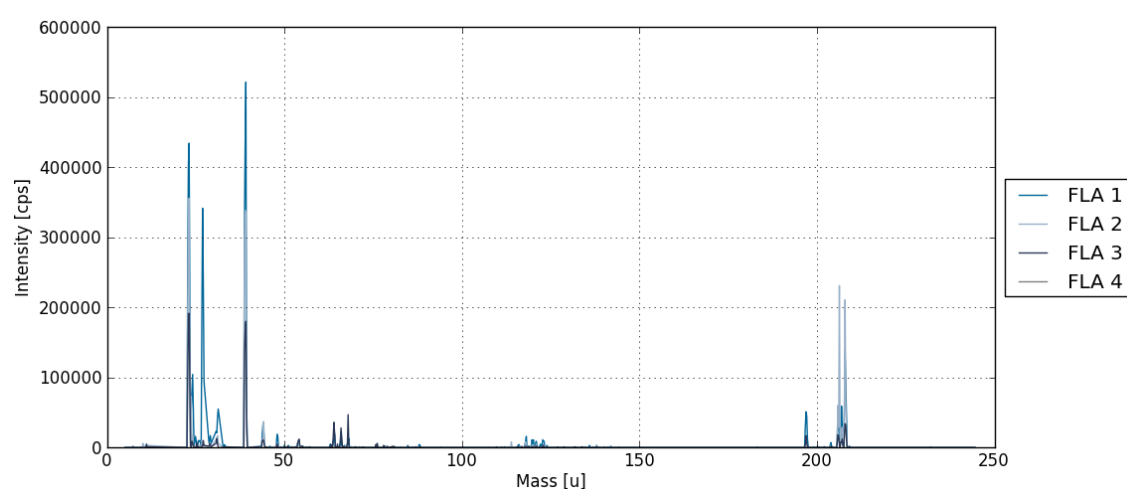
4.3 Linescan measurements

4.3.1 Realization and optimization of linescan measurements

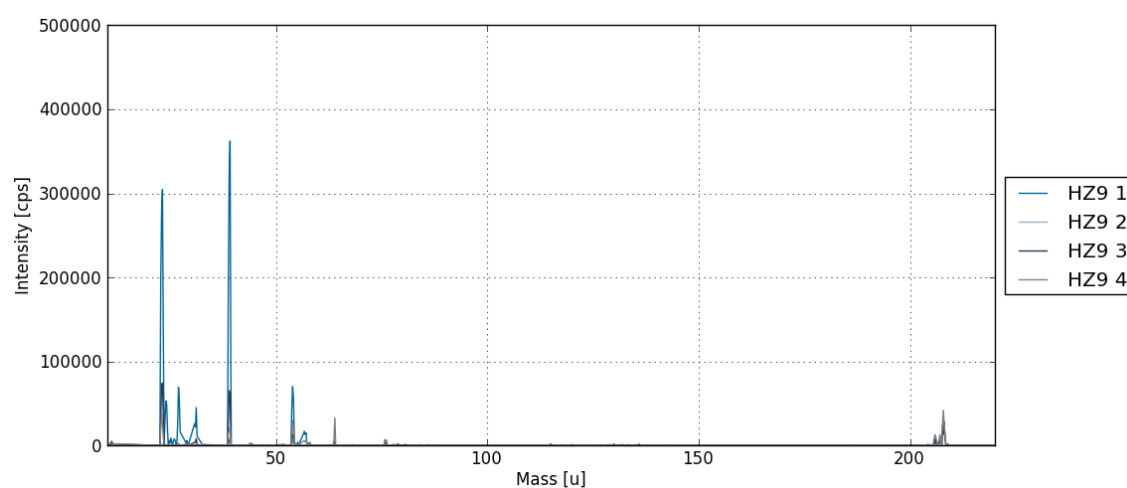
A survey scan was done prior to any linescan experiments to determine the overall sample composition. During this measurement routine the whole mass spectrum was recorded while ablating FLA and HZ9 particles. Four survey runs were executed subsequently while analyzing a single particle. As a result, a spectrum containing peaks at all detected mass-to-charge ratios was obtained. By assigning peaks to certain elements the main

components were identified, in which the intensity of the peak corresponded to the concentration of the element in the fly ash.

In case that different particle sizes exhibited different composition, particle size categories were introduced: 50-80 μm , 80-100 μm , 100-125 μm and three particles per category were analyzed. The survey scan mass spectra for a FLA and HZ9 particle, both with diameters between 80 - 100 μm , are displayed in figure 4.5 (a) and (b). All four of the consecutively ran survey scans are displayed and represent the chemical composition for one particle.



(a) FLA fly ash particle



(b) HZ9 fly ash particle

Figure 4.5: Survey scan mass spectrum for one particle of (a) FLA and (b) HZ9 fly ash

The FLA spectrum in figure 4.5 (a) displayed several recorded signal peaks. The peaks with masses below 50 u were, amongst others, assigned to Na, Mg, Al and K/Ar and Ti. Between 60 and 70 u signals from Cu and Zn were obtained, and around 120 u a response from Sn and Sb. The Au peak from the coating layer at 197 u was clearly visible as well. Pb was responsible for the signals at masses > 200 u.

The mass spectrum for a HZ9 particle is illustrated in figure 4.5 (b). Less peaks were recorded in the mass range < 50 u, still Na, Al and K were present. The signal around 56 u was evidence for iron and also Pb was measured. Peaks from Cu and Zn between 60 and 70 u and Sn and Sb around 120 u were recorded but with less intensity compared to the FLA sample. Finally, no significant differences between size categories were registered. Figure 4.5 displays survey scans from particles with diameters between 80 and 100 μm .

Table 4.3 shows a summary of detected and also relevant analytes from the survey scans. Alkaline and alkaline earth elements were not considered and elements with signal intensity below 1000 cps were registered conditionally.

sample	elements
FLA	Al, Ti, Zn, Cu, Sn, Sb, Pb
HZ9	Al, Fe, Zn, (Sn), Pb

Table 4.3: Results from several survey scans for HZ9 and FLA samples

Based on the survey scan results, linescan measurements were conducted on pre-ablated particles. The laser parameters were set in reference to previously performed experiments (see [45]) and are listed in the following table.

Beam diameter [μm]	10
Repetition rate [Hz]	4
Output [%]	45
Scan speed [$\mu\text{m sec}^{-1}$]	2

Table 4.4: Original linescan parameters

Furthermore, analytes were divided into three categories. ^{27}Al , ^{48}Ti , ^{66}Zn and ^{208}Pb were considered main analytes for the FLA sample, ^{27}Al and ^{208}Pb were recorded as main analytes for HZ9. Secondary analytes included ^{55}Mn , ^{63}Cu , ^{120}Sn and ^{121}Sb for FLA and ^{48}Ti , ^{55}Mn , ^{66}Zn and ^{120}Sn for HZ9. The classification into main and secondary analytes

was done based on signal intensity. ^{197}Au was used to distinguish between sample and mounting base and added as an analyte for all measurements. The measured isotopes are also listed in table 3.3.

Originally, a third category, tertiary analytes was introduced, consisting of ^{53}Cr , ^{54}Cr , ^{111}Cd and ^{114}Cd . These elements were interesting due to their environmental impact but the concentrations were below the detection limit.

During method optimization laserpower, frequency and beam diameter were adjusted to gain the highest possible resolution. Figure 4.6 shows three consecutively recorded linescan measurements for main analytes from the same fly ash particle. The laserpower was either set to 30 % and 45 %, corresponding to a fluence of 0.7 J cm^{-1} and 4.7 J cm^{-1} . The frequency was varied between 4 Hz and 10 Hz.

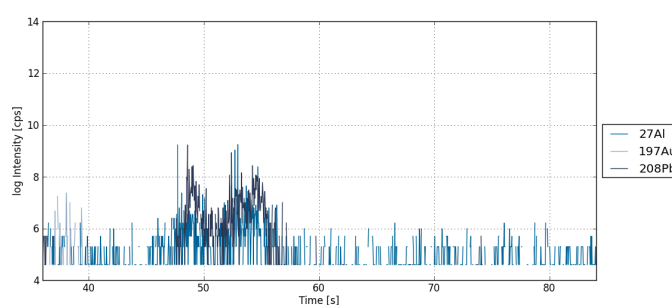
As shown in figure 4.6 (a), a fluence of 0.7 J cm^{-1} was too low to ablate sufficient material as well as the gold background layer. Hardly any response was received for ^{27}Al and ^{208}Pb , not to mention the examination of analyte distributions.

When using a beam diameter of $5\text{ }\mu\text{m}$, it was not until a fluence of at least 4 J cm^{-1} that an adequate signal intensity was reached, as illustrated in figure 4.6 (b). Consequently, an increase in the laser output raised signal intensity. Therefore, a fluence of $5\text{ - }6\text{ J cm}^{-1}$, when using 50 % laserpower was used during further experiments. When measuring secondary analytes, simply the beam diameter was adjusted.

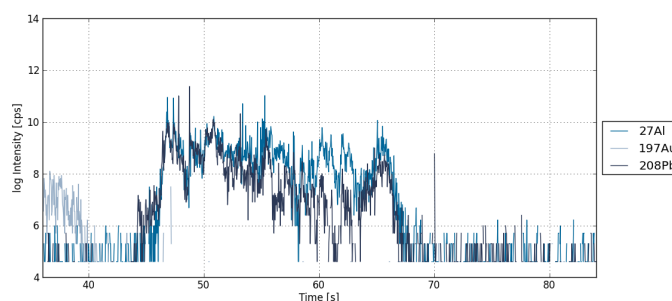
Increasing the frequency at constant laser conditions improved signal intensity and noise but only up to 10 Hz, shown in figure 4.6 (c) . No significant advancement was obtained when employing frequencies $> 10\text{ Hz}$.

Optimized linescan parameters were set to 50 % laserpower, 10 Hz repetition rate, a beam diameter of either $5\text{ or }10\text{ }\mu\text{m}$ and a scan speed of $2\text{ }\mu\text{m sec}^{-1}$. The corresponding fluence and analytes are shown in table 3.3. In general, method development and optimization turned out to be quite delicate. Every particle differed from each other, which made the comparison of obtained signal intensity from a defined set of laser parameters challenging. As a result, a set of at least ten particles was measured for method optimization and trends were elaborated.

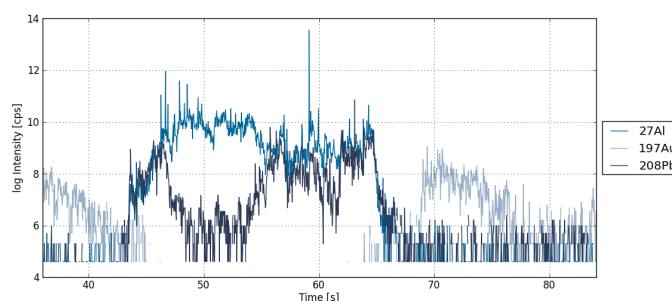
Concerning elemental distribution, figure 4.6 (b) displays a similar signal trend for Al and Pb. Both analytes were distributed throughout the whole surface. Although the signal for ^{208}Pb reaches zero for a short time a distinct core-shell distribution was not obtained. Figure 4.6 (c), on the contrary, shows an inhomogeneous distribution. The aluminium signal stayed constant over the particle surface, while the lead signal decreased in the middle section. This means that differences in elemental distribution were detectable using the optimized laser parameter and a single linescan measurement pattern. Whether or not a core-shell distribution was obtained is discussed later on in chapter 4.3.3.



(a) Linescan laser parameter: 30 %, 10 Hz, 5 μm , 2 $\mu\text{m sec}^{-1}$



(b) Linescan laser parameter: 45 %, 4 Hz, 5 μm , 2 $\mu\text{m sec}^{-1}$



(c) Linescan laser parameter: 45 %, 10 Hz, 5 μm , 2 $\mu\text{m sec}^{-1}$

Figure 4.6: Linescan optimization on (17)_HZ9_<0.5bar_A (Spot 7, 04.02.2015)

4.3.2 Detailed particle analysis through linescan measurements

Elemental distribution on a particles cross-section was initially analyzed using a single linescan. For further examination, several linescans were drawn on one particle. Therefore, variations in horizontal as well as vertical direction became visible. Figure 4.7 shows a schematic illustration of the linescan pattern used to investigate two different FLA fly ash particles. The single linescan was either shifted horizontally and/or rotated for 90°.

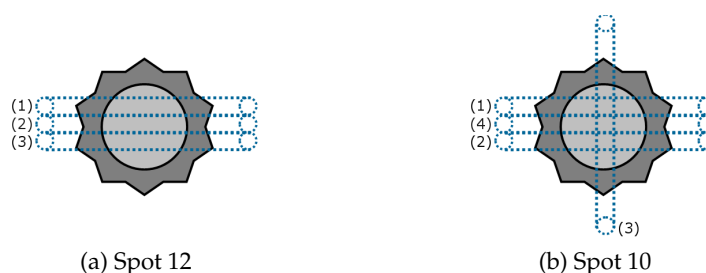


Figure 4.7: Schematic of a linescan pattern used to analyze single particles

Figure 4.8 and 4.9 illustrate the obtained signal intensities from the above pattern. The pattern is displayed on the left-hand side and the associated signal intensities on the right-hand side.

Spot 12 showed varying signal trends when moving the pattern. Figure 4.8 (b) displays a core-shell behavior for Pb and Zn. The Al and Ti signal remained almost constant. In figure 4.8 (d) a decrease in the enrichment of Pb and Zn on the left side of the particle was observed. Still, a core-shell distribution remained. After shifting the linescan pattern once again, an inhomogeneous distribution was observable for all analytes as illustrated in figure 4.8 (f).

Spot 10 on the other hand exhibited a core-shell distribution in all four linescan measurements. Figure 4.9 (b), (d), (f) show the distribution of the main analytes ^{27}Al , ^{48}Ti , ^{66}Zn and ^{208}Pb . Al and Ti were evenly spread, while Pb and Zn signals revealed a higher intensity in the shell of the particle. When shifting the linescan pattern, the same signal trend for all main analytes was obtained. In addition, a core-shell distribution was recorded for the secondary analytes ^{55}Mn , ^{63}Cu , ^{120}Sn and ^{121}Sb . In this context, only the Mn signal remained constant. All the other elements exhibited an enrichment in the outer particle area.

As a result, particle characterisation from only one linescan measurement seemed impractical. The collected signal trends were dependent on the position of the pattern on the surface area which made sample characterisation not representative. The structure of fly ash might be too complex to be determined through analyzing just a fraction of the particles surface.

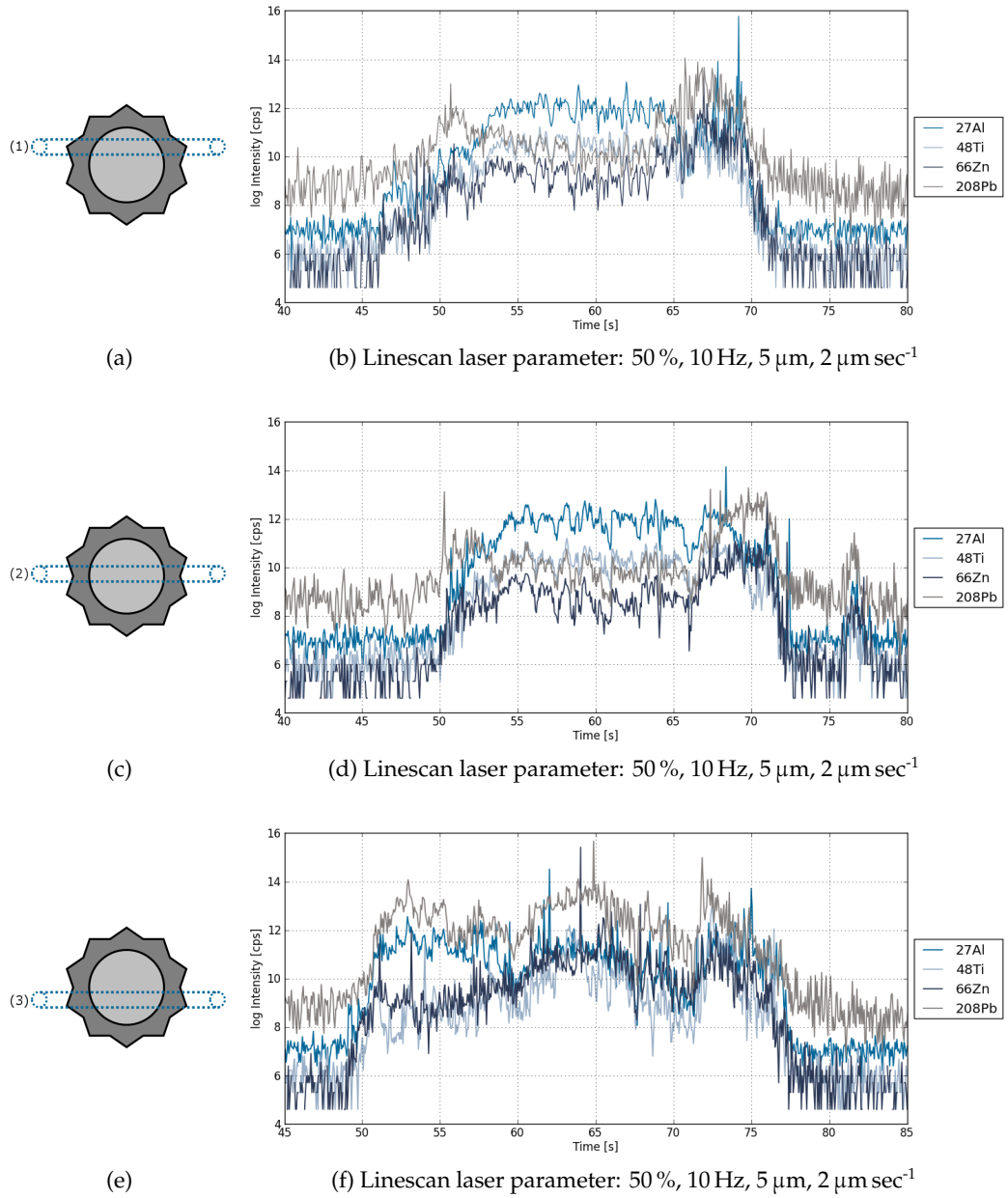


Figure 4.8: (14)_FLA_0.5bar_A (Spot 12, 26.02.2015)

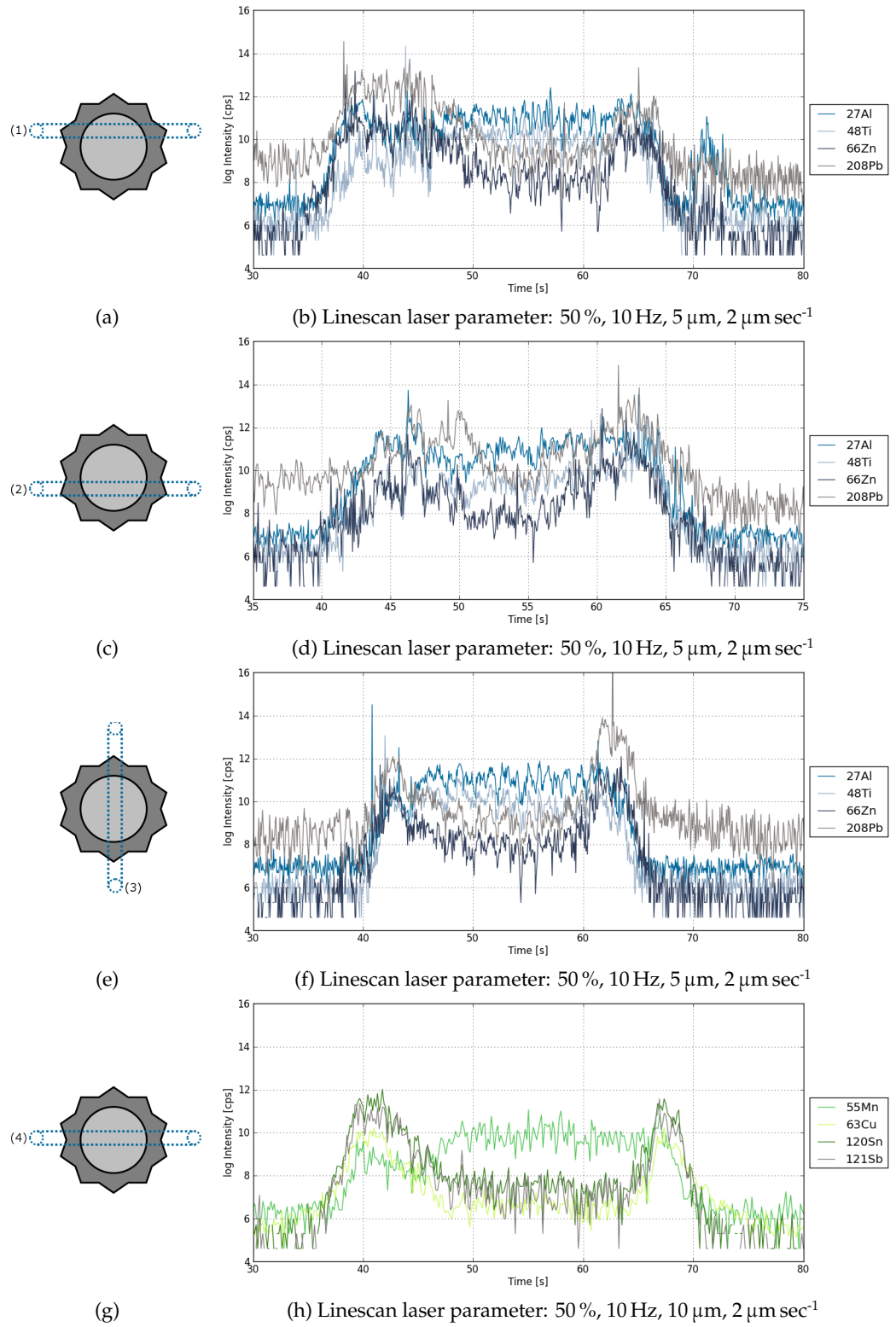


Figure 4.9: (14)_FLA_0.5bar_A (Spot 10, 19.02.2015)

4.3.3 Sample characterisation and résumé

All in all, more than 150 fly ash particles were analyzed using approximately 250 linescan measurements. As already discussed in chapter 4.3.2, characterization of a particle with only one linescan turned out to be impossible due to structural variations on the particles cross-section. Nevertheless, a registration of core-shell elemental distributions was possible. Table 4.5 gives an overview of the number of measured particles and the amount of detected inhomogeneous distributions.

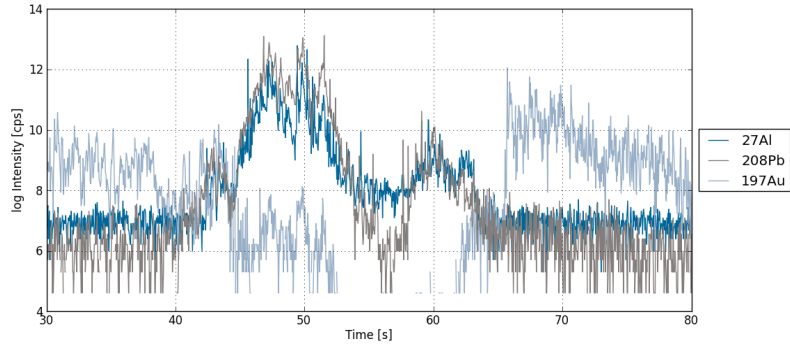
	FLA	HZ9
Number of particles analyzed	68	90
Number of linescans measured	98	140
Number of measured core-shell distributions	13 - 14 %	4 - 9 %

Table 4.5: Linescan measurement statistics

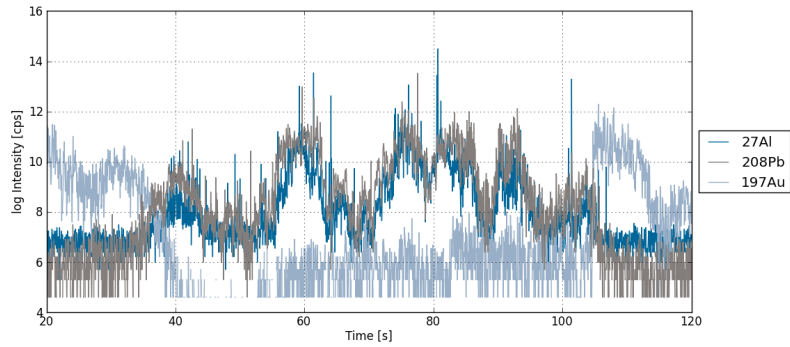
When considering FLA fly ash, 13 - 14 % of the analyzed particles exhibited a core-shell distribution, at least at one of the cross-section linescans. In this connection, signals for Al and Ti showed a homogeneous distribution while Pb and Zn were enriched in the shell of the particle. Informations about secondary analytes were only obtained from a small number of particles, so no accurate prediction about their behaviour can be made.

In contrast to FLA, analysis of HZ9 particles was quite complex. When ten particles were analyzed sometimes 10 different elemental distributions were obtained. Figure 4.10 displays three linescan measurements to illustrate this issue. The signal trends for ^{27}Al , ^{208}Pb and ^{197}Au from the applied gold background layer are displayed. Figure 4.10 (a) shows that Al was present throughout the whole particle in varying concentration while the Pb signal declined in the middle. A core-shell distribution could be assumed for this particle. The presence of an agglomerate was ruled out due to the trend of the Au signal. During the period of 50-70sec, where the particle was ablated, no significant Au signal was detected. Spot 9, presented in figure 4.10 (b) on the other hand, exhibited an inhomogeneous distribution for both, Al and Pb. Again, an agglomerate was ruled out because of the Au signal trend. The beginning and end of the particle were clearly visible. In this case, a core-shell distribution was not applicable, at least not for Pb and Al. No other analyte showed sufficient signal intensity during this measurement.

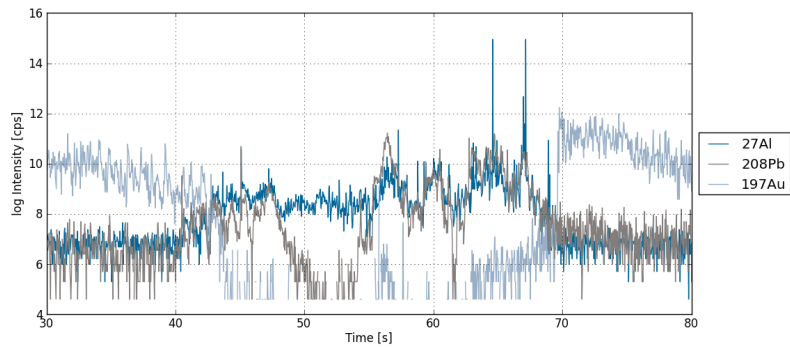
Figure 4.10 (c) represents a combination of signal trends illustrated in (a) and (b). Al was distributed among the whole cross-section with varying concentration. The Pb signal dropped around 50s indicating a core-shell distribution. However, on the right side of the particle the Pb trend fluctuated heavily and dropped down to zero again for a short time. A classification into particles either with a core-shell distribution or with a homogeneous elemental allocation did not seem appropriate.



(a) Spot 4, Linescan laser parameter: 50 %, 10 Hz, 5 μm , 2 $\mu\text{m sec}^{-1}$



(b) Spot 9, Linescan laser parameter: 50 %, 10 Hz, 5 μm , 2 $\mu\text{m sec}^{-1}$



(c) Spot 14, Linescan laser parameter: 50 %, 10 Hz, 5 μm , 2 $\mu\text{m sec}^{-1}$

Figure 4.10: (17)_HZ9<_0.5bar_A (27.02.2015)

In order to compare FLA and HZ9 samples, linescan measurements similar to figure 4.10 (a) and (c) were considered core-shell particles and a yield of 4 - 9 % was received for the HZ9 fly ash. Additionally, two types of particles were observed during laser treatment. Particles were either shiny black or matt black. By trend, matt particles shrank faster under laser exposure and less analytes with lower signal intensity was recorded. As HZ9 samples were received from a blast furnace air pollution system, it was likely that either iron or soot formed the basis of most of the specimen. To distinguish between the main component carbon and iron were added as analytes. While iron was easily detectable at mass 57, measuring carbon with ICP-MS was quite tricky. Carbon is hard to ionize and exhibits a high blank value too. Therefore, the presence or absence of a ^{57}Fe signal was used to classify particles as iron or carbon-based.

Concluding, it can be said that the identification of an inhomogeneous elemental distribution using linescan measurements was possible. Trends for certain elements were discovered, e.g. Pb was enriched in the outer particle sphere while Al was existent throughout the sample cross-section. Nevertheless, one linescan was not enough to determine a particles structure. By shifting linescan pattern on a particle surface different signal trends were obtained. To gain more detailed insight into the structure of fly ash, the measurement of elemental distributions across the whole cross-section was necessary. The categorization into either core-shell particles or particles without a core-shell structure had to be reconsidered as well.

4.4 Image measurements

Imaging experiments using LA-ICP-MS were conducted to advance the analysis of fly ash particles. By scanning the whole cross-section, space-resolved information about the elemental distribution was obtained. The previously performed linescan measurements served as reference for adjusted laser parameters. The optimized parameters and analytes are listed in table 3.4 in chapter 3.4.3.

Although the analytes were separated into main analytes and secondary analytes during linescan experiments, only one measuring cycle was practicable when recording

an image. As every particle was unique, choosing particular elements was not feasible. Moreover, adding analytes after the experiment is impossible in ICP-MS. As a result, all main and secondary analytes were put into one measuring sequence. The signal intensities were checked after the recording for each image and the signal-to-noise ratio had to reach at least a value of 2 - 3.

Furthermore, the initial laser conditions were varied to improve spatial resolution. When reducing the beam diameter, a decreased amount of material gets ablated which may prohibit the detection of less concentrated analytes. To prevent latter from happening, the fluence was increased when measuring with a smaller laser diameter. Table 4.6 shows the laser parameters and the associated fluence values for all tested conditions.

Laser parameters	1	2	3	4
Beam diameter [μm]	5	3	3	3
Repetition rate [Hz]	20	10	20	20
Output [%]	50	50	60	80
Scan speed [$\mu\text{m sec}^{-1}$]	3	3	3	3
Fluence [J cm^{-2}]	5 - 6	4 - 5	8 - 9	17 - 18

Table 4.6: Tested laser conditions during LA-ICP-MS imaging experiments

Looking at table 4.6, a beam diameter of $5\mu\text{m}$ and the laser settings from column 1 were considered standard settings. A reduced beam diameter of $3\mu\text{m}$ was tested in combination with three different laser parameters and fluences. Column 2 represents the same laser conditions as in column 1 with a decreased diameter. Therefore, the fluence diminished as well. Column 3 and 4 display laser adjustments with increased laser power and fluence with a $3\mu\text{m}$ beam diameter. As already explained, reducing the beam diameter influences the amount of mass ablated and as a result the detection limit of less concentrated elements. Images using LA-ICP-MS were measured using every set of laser parameters listed in table 4.6. It was discovered that sufficient signal intensity was recorded for FLA and HZ9 samples. Especially the detection of considered main analytes Al, Ti, Zn and Pb for FLA and Al and Pb for HZ9 was no problem.

The time-resolved intensities for the measured isotopes were recorded with the Qtegra software and exported as .csv files. Afterwards, the files were imported into the ImageLab software for further processing. The scanning mode (line or plot scan) and the scan

direction were selected through the user interface. The vertical number of pixels was automatically calculated and set to the number of detected lines whereas the horizontal resolution could be set manually. During data import, the time-resolved signal was divided into individual regions by the software algorithm. The length of the region was dependent on the laser beam diameter and the scan speed. Then, the signal of one period was averaged to obtain the numeric value for a single pixel. Elemental images were created in which the signal intensity of the measured isotope of a defined region corresponded to the color of a pixel. The software also allowed for correction to internal standards and the overlay of an elemental distribution and an image acquired from optical microscopy or SEM. All constructed images exhibited a resolution of either 24 x 24 px for a 5 μm beam or 40 x 40 px for a 3 μm laser diameter and displayed an area of 120 x 120 μm .

An example is given in figure 4.11. The elemental distribution of ^{27}Al , ^{57}Fe and ^{208}Pb of a HZ9 fly ash particle is shown. The brighter the pixel, the higher the concentration of the element in the particle. The correlation of LA-ICP-MS signal intensity and the color of the pixel is plotted in the scale below the image. It has to be pointed out that the same pixel color in a different elemental distribution corresponds to different signal intensities and concentrations.

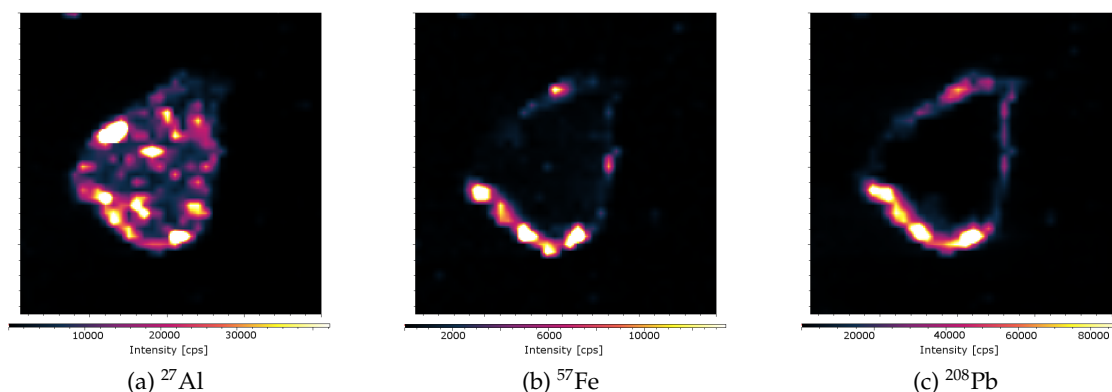


Figure 4.11: Evaluated imaging experiment using ImageLab software,
(17)_HZ9_<0.5bar_A, Spot 7, Laser parameter: 80 %, 20 Hz, 3 μm ,
3 $\mu\text{m sec}^{-1}$, 22.04.2015

Altogether, 27 FLA particles and 10 HZ9 particles were analyzed through LA-ICP-MS imaging. In general, when examining the HZ9 fly ash less elements were detectable compared to FLA samples. As already discovered during linescan measurements, this

was due to the assumed main components iron and soot. Measurable elements were often located on the surface with barely any signal from the core of the particle indicating that most of the specimen were formed through abrasion. In addition, the measured particles did not represent ideal spheres and adsorption and condensation took place on specific surface regions. A classification into core-shell and non-core-shell particles seemed too simple for the obtained, complex elemental images.

To determine the accuracy of the LA-ICP-MS images and verify the measured signal trends a validation process had to be introduced as a next step. As it turned out, a beam diameter of 3 μm with a fluence less than 17 - 18 J cm^{-2} produced a wrong elemental distribution. Method validation and image optimization is discussed in greater detail in the following chapter 4.5.

4.5 Method validation using SEM-EDX

Using LA-ICP-MS for elemental mapping of fly ash particles provided significant results. Elemental images for main and trace components were obtained. However, method verification was necessary to identify spectral interferences or elemental fractionation and to check the adjusted laser conditions. SEM turned out to be the method of choice, offering two distinctive benefits over optical microscopy:

- SEM offers high spatial resolution to gain insight into optical structures of fly ash particles.
- At the same time, identification of main components and their elemental distribution is possible through EDX measurements.

Although SEM in combination with x-ray spectroscopy provided the necessary features to validate LA-ICP-MS results, one distinct difference between the two techniques has to be kept in mind: in x-ray spectroscopy only the top atomic layers were excited in contrast to laser ablation where several μm of material were removed. Depending on the particle structure differing images may potentially be received from both methods.

The conducted procedure to verify the laser based results can be explained as follows: Since it was possible to attach a picture to the elemental mapping created with the

ImageLab software, SEM images were taken and adjusted to the size and orientation of the LA-ICP-MS data matrix. Consequently, it was possible to gain information about structural variations and compare them with elemental distributions. In order to receive information about the surface structure, SEM images had to be taken before LA-ICP-MS imaging experiments. As already explained in chapter 3.5, the particles were pre-ablated and labelled with the laser first. Then the SEM analysis of the same particle was done before LA-ICP-MS imaging.

Selected fly ash particles from the FLA sample are shown in figure 4.12. As it can be seen, different structures were visible. Spot 1 exhibited a flat, uniform surface with crumb-like smaller particles arranged at the outer area. Spot 3 on the other hand looked like an agglomerate of smaller and middle-sized particles. Spot 2 represented a mixture of both structural characteristics. Smaller, single particles were clearly visible as well as bigger, flatlike areas. In general, FLA particles showed at least one of the structural characteristics mentioned above. The prepared cross-sections were a combination of crumb-like structures, smaller, single particles and bigger, flat areas looking like molten metal or glass. Nevertheless, every particle was unique and these pictures should only display the observed structural variety.

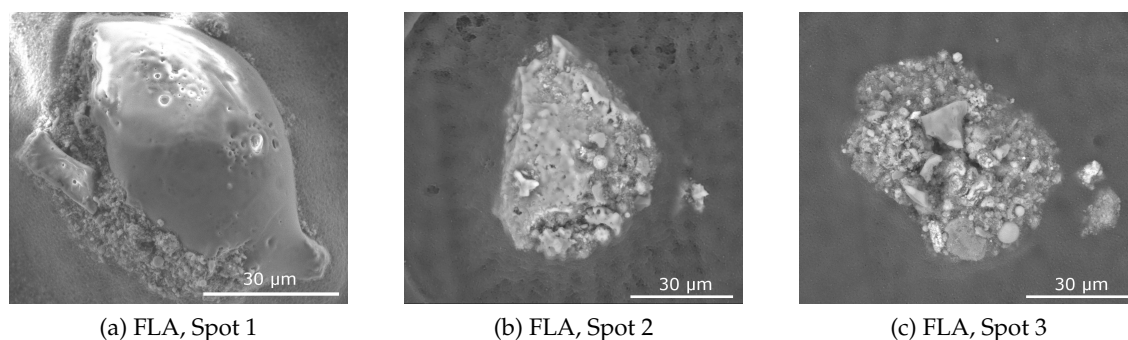


Figure 4.12: Pictures from selected FLA fly ash particles obtained from secondary electrons (SE), sample (14)_FLA_0.5bar_A

The SEM pictures of the HZ9 sample confirmed the presence of two different main components which were visually distinguishable. Supposed iron particles were composed of an agglomerate of many smaller particles while carbon-containing particles exhibited a smooth, uniform surface. Examples are illustrated in figure 4.13, showing an iron particle on the left-hand side and a carbon particle on the right-hand side.

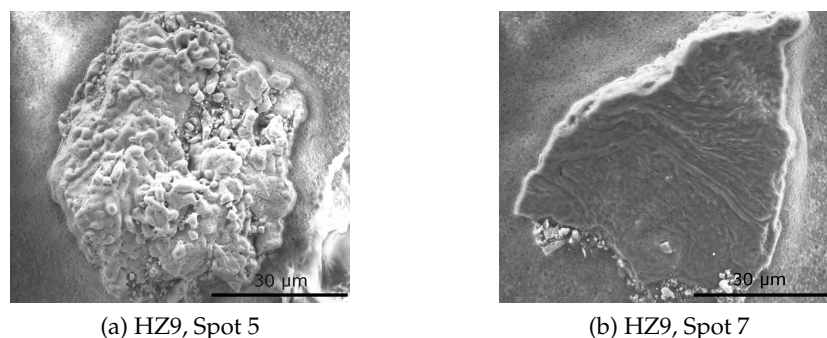


Figure 4.13: Pictures from selected HZ9 fly ash particles obtained from secondary electrons (SE), sample (17)_HZ9_<0.5bar_A

The next task during method verification was to determine analytes detectable with SEM-EDX as well as LA-ICP-MS. When using signals obtained from both techniques a comparison of elemental distributions was possible. The benefit of EDX analysis in this case was that it was possible to select elements after performed measurements because the whole spectrum was recorded. Despite that, some considerations have to be kept in mind: only elements with a concentration > 0.1 w% were traceable with EDX measurements and comparable analytes were limited to those detectable with the laser. A list of comparable analytes for FLA and HZ9 samples is shown in table 4.7, if ideal conditions concerning particle structure and concentration were met.

fly ash sample	comparable elements
FLA	Al, Si, Ti, Zn
HZ9	Al, Fe

Table 4.7: Comparable analyte signals from LA-ICP-MS and EDX

When analyzing FLA samples with laser ablation, adequate signal intensities were received for ^{27}Al , ^{48}Ti , ^{63}Cu , ^{66}Zn , ^{120}Sn , ^{121}Sb and ^{208}Pb . The isotope ^{29}Si was also measured but the signal exhibited a very high background and only certain particles contained enough Si to produce an adequate increase in signal intensity. During EDX-measurements, it was discovered that the most intense emission line for Pb was overlapped by a sulfur signal and the concentration of Pb was too low to switch to another spectral region. Additionally, Sn and Sb signals were overlapped by Ca which turned out to be a main component of FLA fly ash and the Cu-concentration was too low to obtain

an EDX signal. As a result, no data concerning Pb, Sn, Sb and Cu was received using EDX analysis. These circumstances yielded in the list of analytes given in table 4.7.

While investigating HZ9 samples, signals trends for ^{27}Al , ^{48}Ti , ^{55}Mn , ^{57}Fe , ^{66}Zn , ^{120}Sn and ^{208}Pb were recorded with LA-ICP-MS. As concentration of analytes besides the main components iron and soot was low, receiving EDX data was only possible for Al, Fe.

To summarize, elements which exhibited satisfactory signal intensity in LA-ICP-MS and during EDX measurements were dependent on the particle structure and composition. The identification and comparison of suitable analytes had to be done for every specimen. In some cases, the verification of four or more laser ablations signals per particle was possible, in other cases the comparison of none or only one elemental trend was feasible. Nevertheless, it was assumed that if the LA-ICP-MS elemental distribution of one particle was confirmed by EDX data, the laser obtained signals from other particles were reliable as well.

To illustrate the described procedure, figure 4.14 shows the distribution of Al over the prepared cross-section of a FLA particle with the laser-based signal for ^{27}Al on the left-hand side and the EDX mapping for Al on the right-hand side. Hence, a SEM picture of the particle was overlapped by the obtained measurement data from both techniques using the ImageLab software. The signal range was assigned to a color scale, whereat the brighter the color, the higher the measured concentration. As immediately apparent, elemental distribution was not identical. When evaluating EDX measurement data, Al was found evenly distributed throughout the cross-section as displayed in 4.14 (b). Only a small area in the middle exhibited no Al content. As it can be seen in figure 4.14 (a), when using signals received from LA-ICP-MS, Al was only discovered in the crumb-like outer particle area. As the elemental images from both methods did not match, the difference could be explained by the applied laser conditions in LA-ICP-MS. Obviously, the adjusted laser power was too low for sufficient mass removal. When using a beam diameter of only $3\text{ }\mu\text{m}$, as tested in this case, a fluence of $8\text{--}9\text{ J cm}^{-2}$ was inadequate. As a result, these laser conditions were discarded.

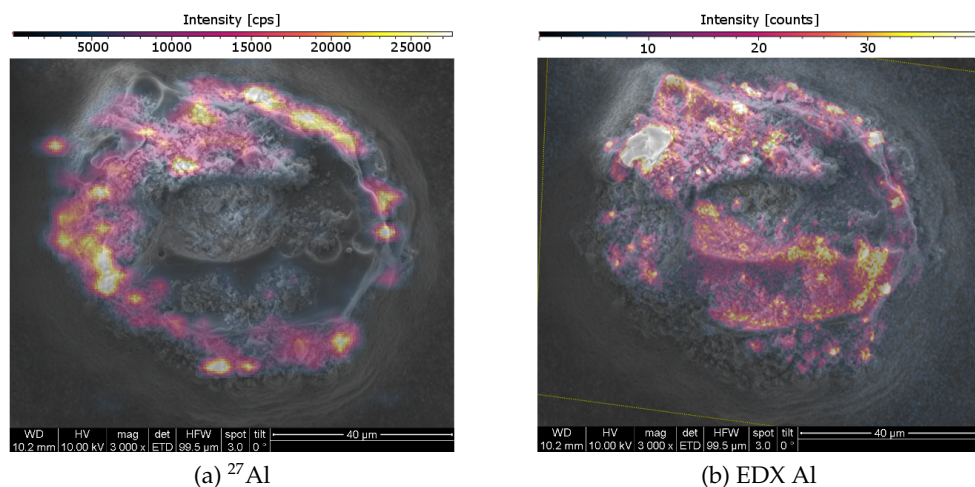


Figure 4.14: Comparison of elemental imaging using LA-ICP-MS and SEM-EDX, FLA, Spot 8, Laser parameter: 60 %, 20 Hz, 3 μm , 3 $\mu\text{m sec}^{-1}$, 05.05.2015

The same procedure was carried out using data from measurements with different laser adjustments. In this way, it was possible to optimize and verify every set of laser parameters. LA-ICP-MS settings that produced results which were not in agreement with the EDX image led to the increase of laser power and fluence values. A summary of all tested laser parameters is listed in table 4.6. Using a beam diameter of 5 μm with a fluence of 5-6 J cm^{-2} turned out to provide reliable data for FLA and HZ9 particles. When decreasing the laser diameter to 3 μm , a fluence of 17-18 J cm^{-2} was necessary to obtain safe results.

After the examination and verification of elemental distributions, gaining information about structural changes due to laser treatment became interesting. The influence of enhanced fluence values when diminishing the laser beam diameter was of particular concern. Hence, SEM investigation of already lasered fly ash particles was performed. An example of treated particles with different laser power intensities is given in figure 4.15.

Figure 4.15 (a) shows a particle ablated with the lowest applied fluence. Little impact from the laser was visible on the surface, and the signal intensity during laser ablation was very low. Moreover, analytes were only detectable in the agglomerated section of the particle on the lower left side but not in the molten area in the middle with LA-ICP-MS.

A fluence of $4-5 \text{ J cm}^{-2}$, corresponding to a laser power of 50 % and a beam diameter of $3 \mu\text{m}$ already turned out to be insufficient when comparing LA-ICP-MS and SEM-EDX data. Figure 4.15 (a) illustrates why.

A particle examined with a fluence of $6-7 \text{ J cm}^{-2}$, resulting from the standard laser settings 50 % output and $5 \mu\text{m}$ beam diameter is shown in figure 4.15 (b). The effect of laser treatment was clearly visible but the basic particle was still existing. Previously observed cross-section structures were vanished.

Spot 3 was analyzed applying the highest tested fluence of $17-18 \text{ J cm}^{-2}$ when using a beam diameter of $3 \mu\text{m}$. Although LA-ICP-MS imaging experiments provided reasonable elemental distributions, the particle was almost completely ablated. An additional measurement cycle, performing pre-ablation and imaging to obtain a 3-D model would not be possible. As a consequence, a fluence of $17-18 \text{ J cm}^{-2}$ was considered too high for the following experiments.

The optimized imaging conditions were therefore set to a beam diameter of $5 \mu\text{m}$ with a corresponding fluence of $6-7 \text{ J cm}^{-2}$.

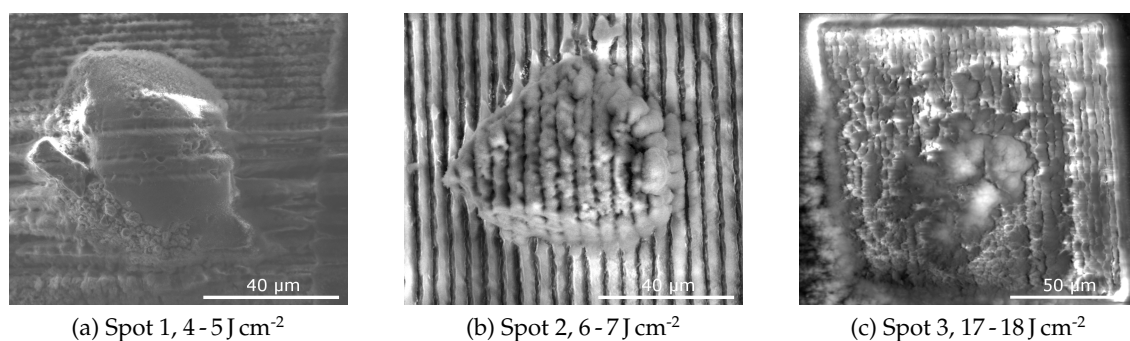


Figure 4.15: Pictures from selected fly ash particles obtained from secondary electrons (SE) after laser treatment

In conclusion, SEM and EDX measurements provided a powerful tool to validate the performed LA-ICP-MS imaging experiments. Additionally, insights into detailed particle structure were enabled. By combining information from both techniques a precise analysis of a single particle was possible. Main components were identified using EDX data while secondary components were measured with LA-ICP-MS.

Due to diverging ranges of influence, the recorded elemental distributions from both techniques might vary. During laser treatment several μm of material got ablated. When

performing EDX measurements only the top atomic layers were excited. Despite that, a good accordance of signals from both methods was obtained which made SEM-EDX the perfect technique to complete particle information received from LA-ICP-MS.

4.6 FLA sample characterisation

Using SEM-EDX analysis and LA-ICP-MS, 27 FLA fly ash particles were characterized. The combination of data obtained from both techniques allowed the identification of main and secondary analytes, the observation of structural differences and the illustration of elemental distributions.

It was found out, that fly ash particles exhibited complex structures emerged from the combination of crumb-like arrangements, agglomerates of individual, middle-sized particles and bigger, flat structures looking like melt. These visually observable differences were recovered when examining the elemental distribution of certain analytes.

The main components were determined using EDX analysis. Ca, O, Al, Si and to a lesser extent S and Mg were considered the most important ones. Ca, O, and S were present throughout the whole particle cross-section. Al and Si were homogeneously distributed as well but accumulation in molten-looking areas and isolated particles was observable. Additionally, it was possible to identify single, isolated particles within agglomerates consisting of iron or MgCl_2 for example.

During LA-ICP-MS signal trends for ^{27}Al , ^{29}Si , ^{48}Ti , ^{63}Cu , ^{66}Zn , ^{120}Sn , ^{121}Sb and ^{208}Pb were recorded. The obtained elemental distribution from main components like ^{27}Al and ^{29}Si but also from ^{48}Ti and ^{66}Zn were used to compare signal trends with EDX mappings. The other analytes provided additional data for sample characterisation.

Examples of measured FLA fly ash particles are presented in figures 4.16 and 4.17. To compare results from LA-ICP-MS and EDX measurements, signal trends obtained from laser imaging are displayed on the left-hand side while EDX mappings are displayed on the right-hand side. Data from both techniques was processed using the ImageLab software.

FLA Spot 2 is illustrated in figure 4.16. A comparison of the distribution of Al, Si, Zn and Ti was possible and the signal trends from both methods agreed well with each

other. Al and Si were distributed over the whole surface with punctual accumulations. These were attributed to two smaller particles on the right side. Although the obtained image from laser ablation only exhibited 24×24 pixels, the enrichment was visible when observing the Al signal. As LA-ICP-MS was the more sensitive method, Al and Si were found throughout the whole surface. Zn and Ti were unevenly distributed but the signal trends from SEM-EDX and laser ablation matched. Consequently, the obtained data from laser ablation was verified (laser parameter: 50 %, 20 Hz, $5 \mu\text{m}$, $3 \mu\text{m sec}^{-1}$) and signals acquired from both techniques provided additional information. To supplement the findings, Sn and Pb were only present in two small spots on the particles' surface. Ca, Mg and O formed the basis of the particle.

Another FLA fly ash sample, Spot 3, is displayed in figure 4.17. Similar to Spot 2, matching analyte distributions for LA-ICP-MS and EDX data were found for Al, Si, Zn and Ti. The surface structure of Spot 3 exhibited various smaller, isolated particles within the cross-section. These structural changes were reflected in the elemental distribution too. Al was present in the bulk of the particle as well as in the smaller, isolated middle structure. Si on the other hand, was concentrated in certain areas as well as Ti. Zn was present everywhere except in the middle structure. The elemental distribution of Sn, Sb and Pb was discovered using laser ablation as the concentrations were too low for EDX. These analytes showed a similar behaviour as Zn. Matrix components like Ca and Mg were detected using SEM-EDX. There was one area on the particles' right side, a round sponge-like structure which consisted of Mg and Cl. Both analytes were not measurable with laser ablation, and therefore no signal was detected around this specific area. As elemental distributions obtained from LA-ICP-MS agreed with EDX measurements, the applied laser settings (Laser parameter: 80 %, 20 Hz, $3 \mu\text{m}$, $3 \mu\text{m sec}^{-1}$) were verified. Although the beam diameter was set to $3 \mu\text{m}$, reliable results were provided. This was due to the increase in laser power and fluence ($17\text{--}18 \text{ J cm}^{-2}$). As already discussed in chapter 4.5, an increased fluence lead to increased ablation of material. A picture of this specific particle after laser treatment was illustrated in figure 4.15(c) and showed that the particle was almost completely removed. This resulted in the rejection of the tested laser adjustments although the received elemental images were satisfactory.

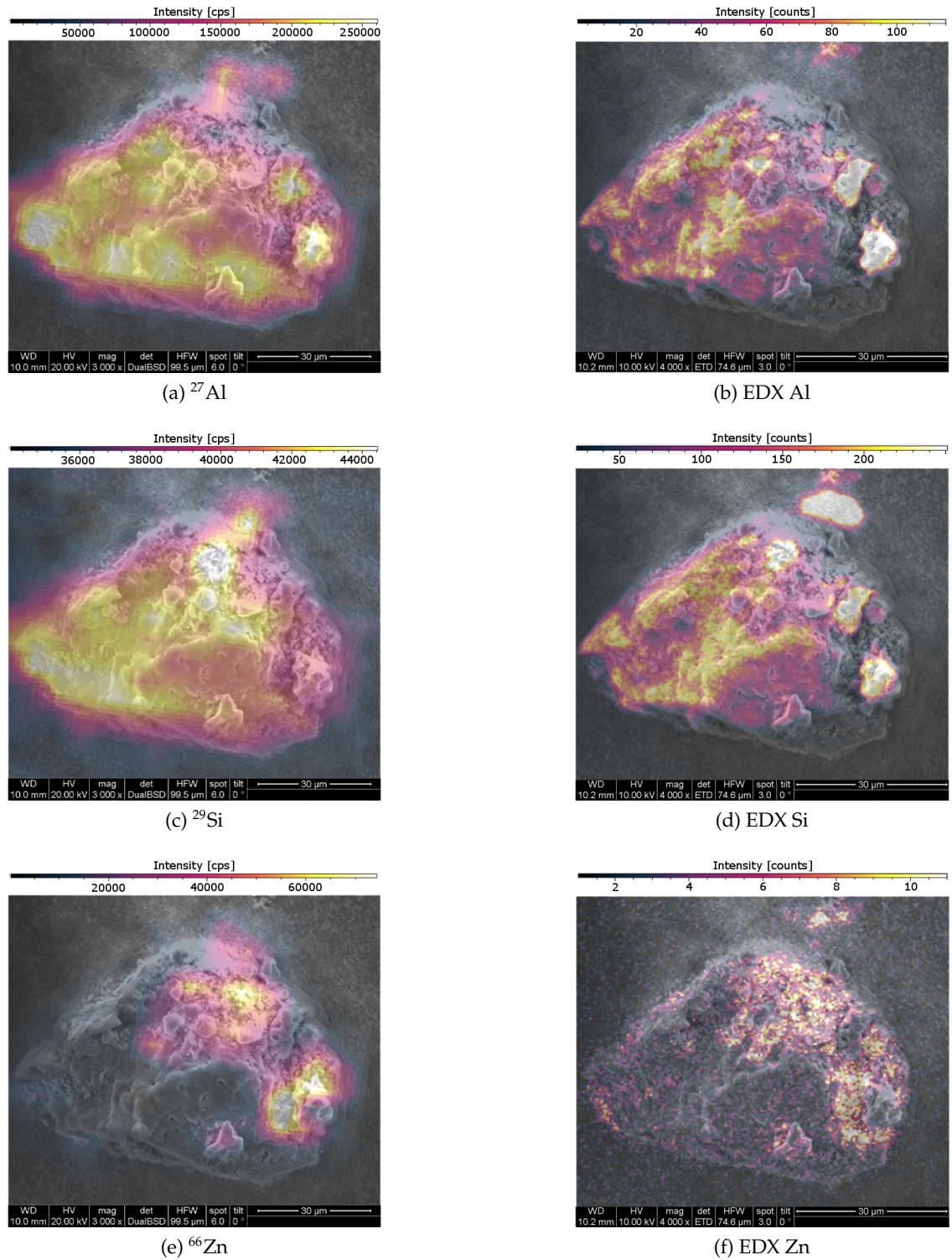


Figure 4.16: Comparison of elemental imaging using LA-ICP-MS and SEM-EDX, FLA, Spot 2, Laser parameter: 50 %, 20 Hz, 5 μm , 3 $\mu\text{m sec}^{-1}$, 15.04.2015

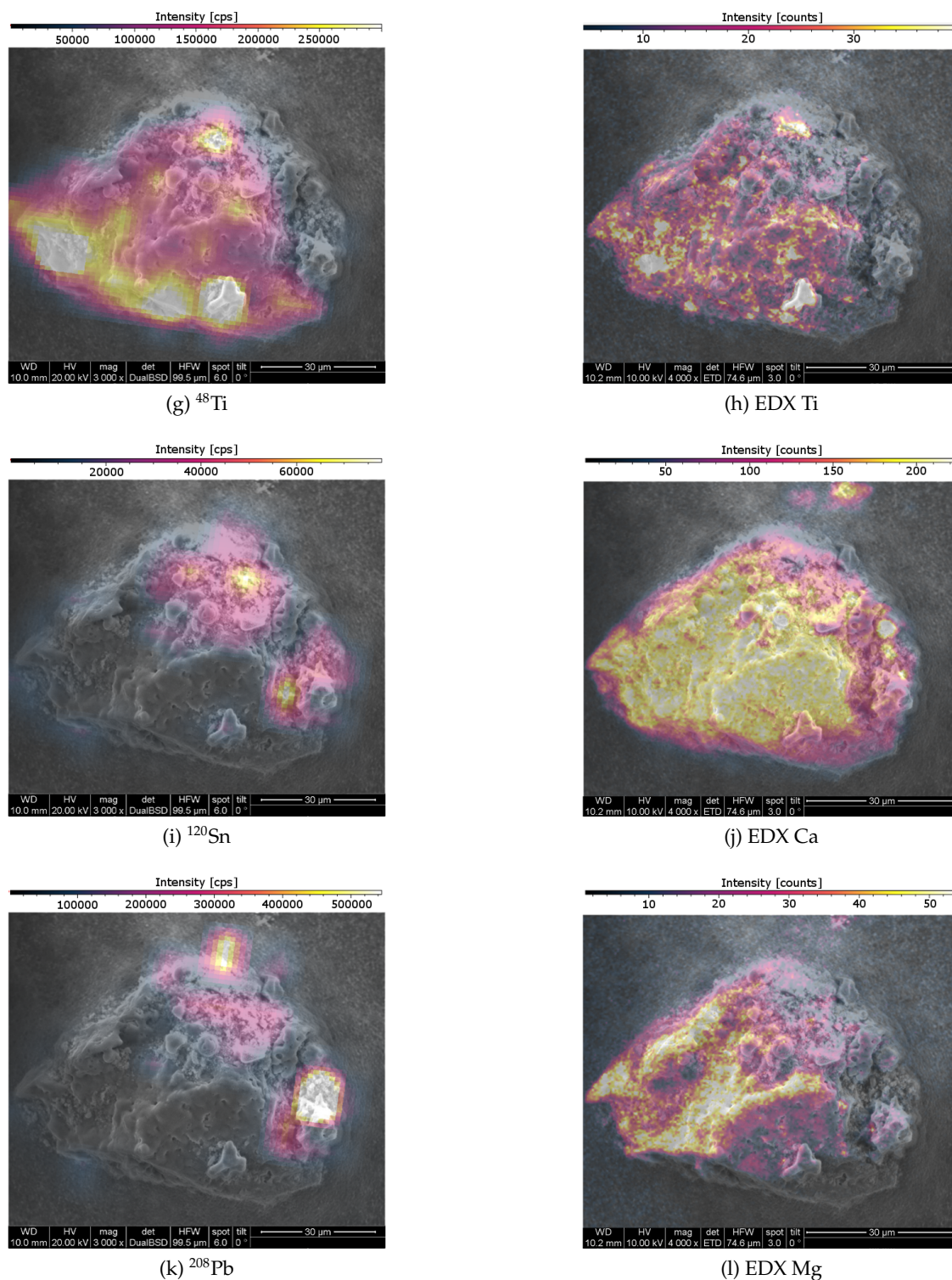


Figure 4.16: Comparison of elemental imaging using LA-ICP-MS and SEM-EDX, FLA, Spot 2, Laser parameter: 50 %, 20 Hz, 5 μm , 3 $\mu\text{m sec}^{-1}$, 15.04.2015

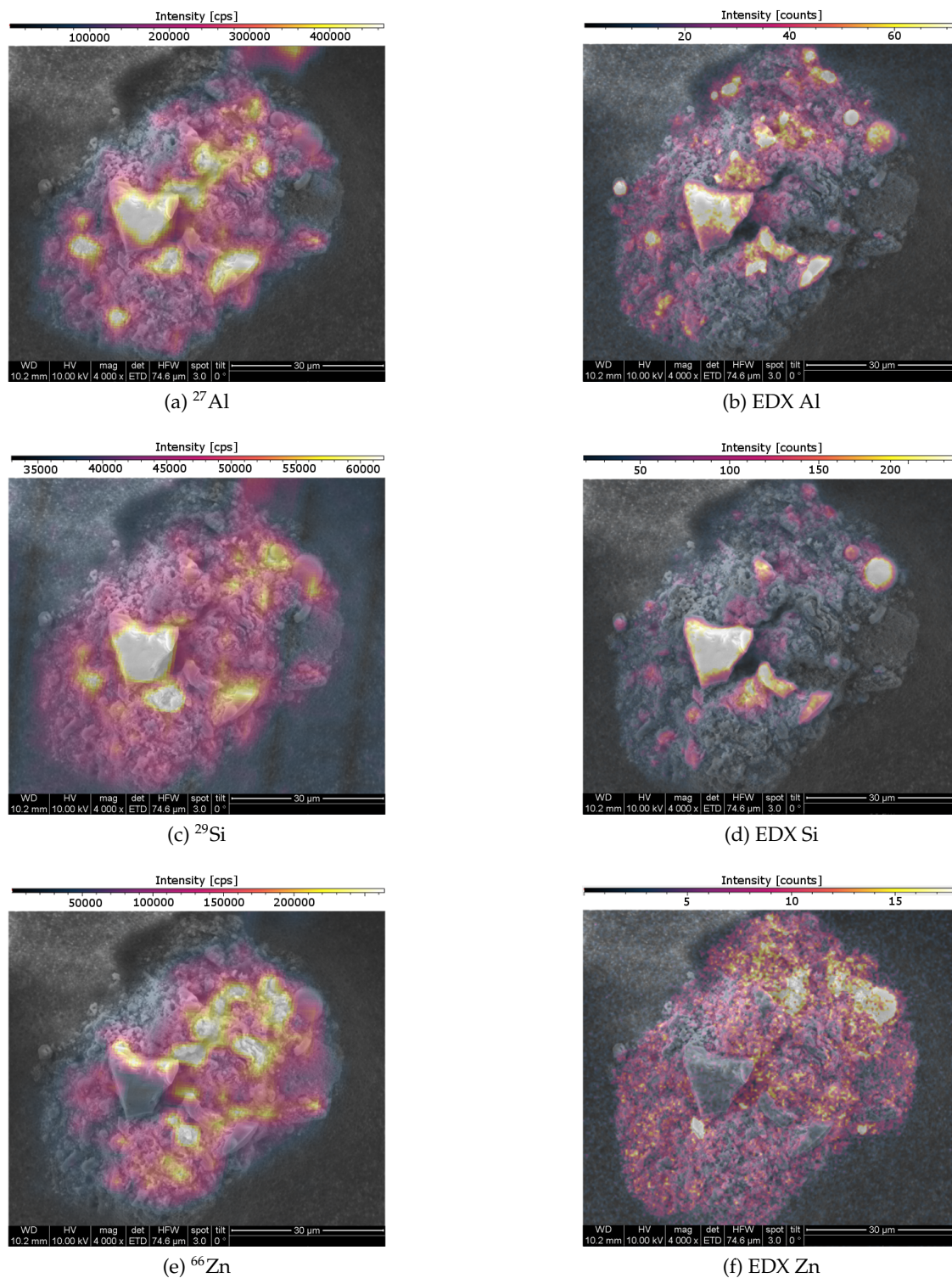


Figure 4.17: Comparison of elemental imaging using LA-ICP-MS and SEM-EDX, FLA, Spot 3, Laser parameter: 80 %, 20 Hz, 3 μm , 3 $\mu\text{m sec}^{-1}$, 15.04.2015

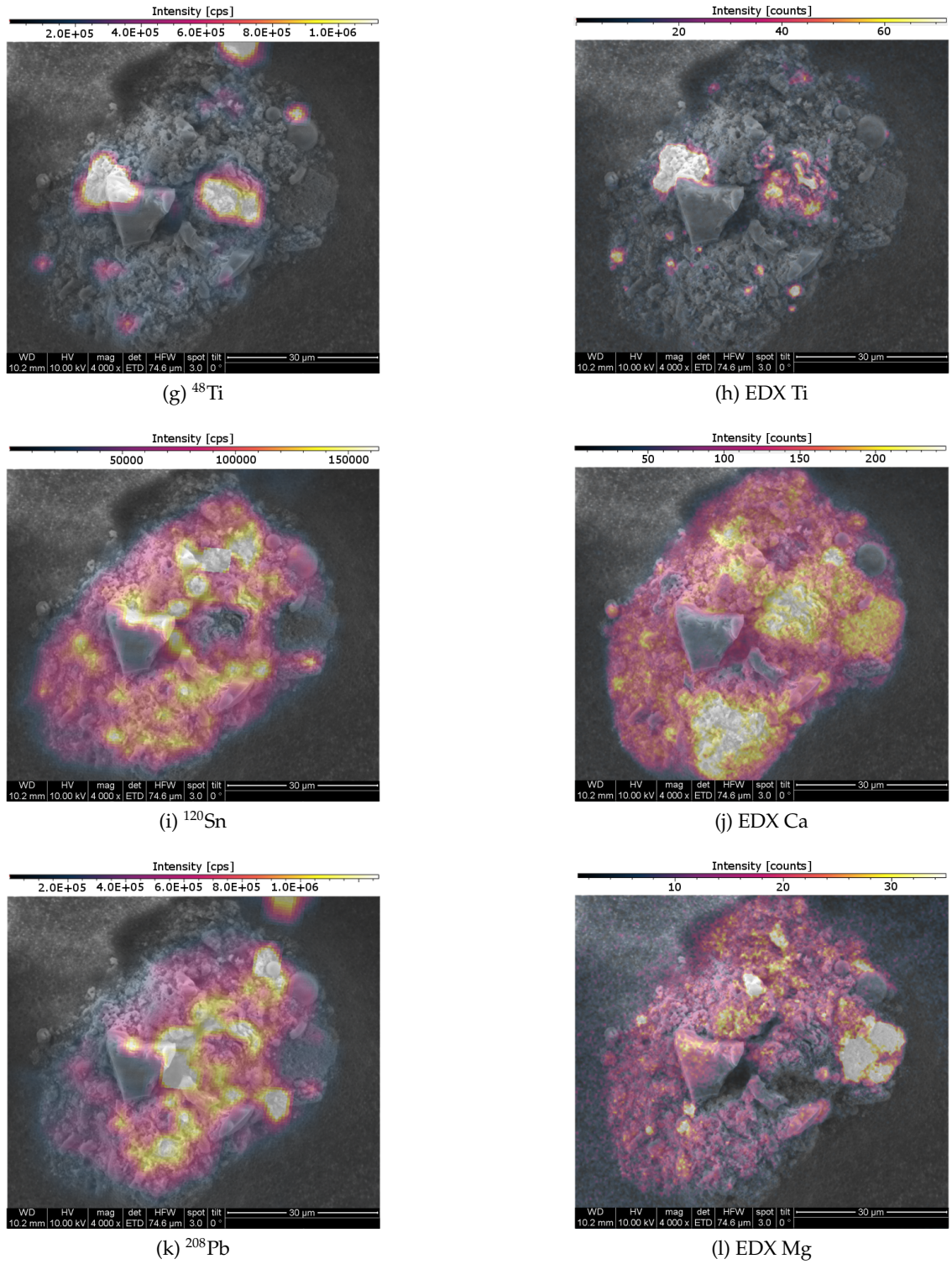


Figure 4.17: Comparison of elemental imaging using LA-ICP-MS and SEM-EDX, FLA, Spot 3, Laser parameter: 80 %, 20 Hz, 3 μm , 3 $\mu\text{m sec}^{-1}$, 15.04.2015

4.7 HZ9 sample characterisation

Besides FLA fly ash also 10 HZ9 particles were analyzed. For that purpose, laser parameters were adopted from FLA measurements. Again, SEM-EDX offered the ability to observe surface structures and the illustration of the chemical composition of a particle was done combining data from both techniques.

In general, HZ9 fly ash samples exhibited less complex structures and chemical components compared to FLA. The presence of two different main components, iron and soot was visually distinguishable and confirmed by LA-ICP-MS and EDX. The surface of iron-based spots looked like an agglomerate of small, round particles while carbon-based samples exhibited a smooth, uniform cross-section. The discrimination into iron- and soot-based particles was done using EDX mappings of Fe and C or by the absence or presence of a ^{57}Fe signal in ICP-MS.

As the concentration of other elements was low, gaining additional information from SEM-EDX and LA-ICP-MS was tricky. During LA-ICP-MS analysis, signals for ^{27}Al , ^{48}Ti , ^{55}Mn , ^{57}Fe , ^{66}Zn , ^{120}Sn and ^{208}Pb were recorded. In general, Al and Ti were incorporated in carbon particles and Fe deposits were found on the particle sphere. When analyzing iron samples, secondary analytes were enriched punctually at outer particle areas while Ca, O, and Si were distributed homogeneously across the cross-section.

Examples of measured HZ9 fly ash particles are presented in figures 4.18 and 4.19. Signal trends obtained from laser imaging are displayed on the left-hand side while EDX mappings are displayed on the right-hand side. The data obtained from both techniques was processed and displayed using the ImageLab software.

Figure 4.18 shows the elemental distribution on a carbon particle. LA-ICP-MS signals for ^{27}Al and ^{57}Fe were compared with EDX data and did agree well with each other. No other element was present with sufficient concentration to receive an EDX mapping. The only additional data was obtained from laser experiments indicating that Pb was present at the edges while Ti was distributed over the whole cross-section.

Figure 4.19 represents an iron-based particle. Fe and O were considered the main components, indicated by EDX measurements. Additionally, traces of Ca and Si were found. All other elements, detected by LA-ICP-MS were located at the outer particle area with quite similar distributions.

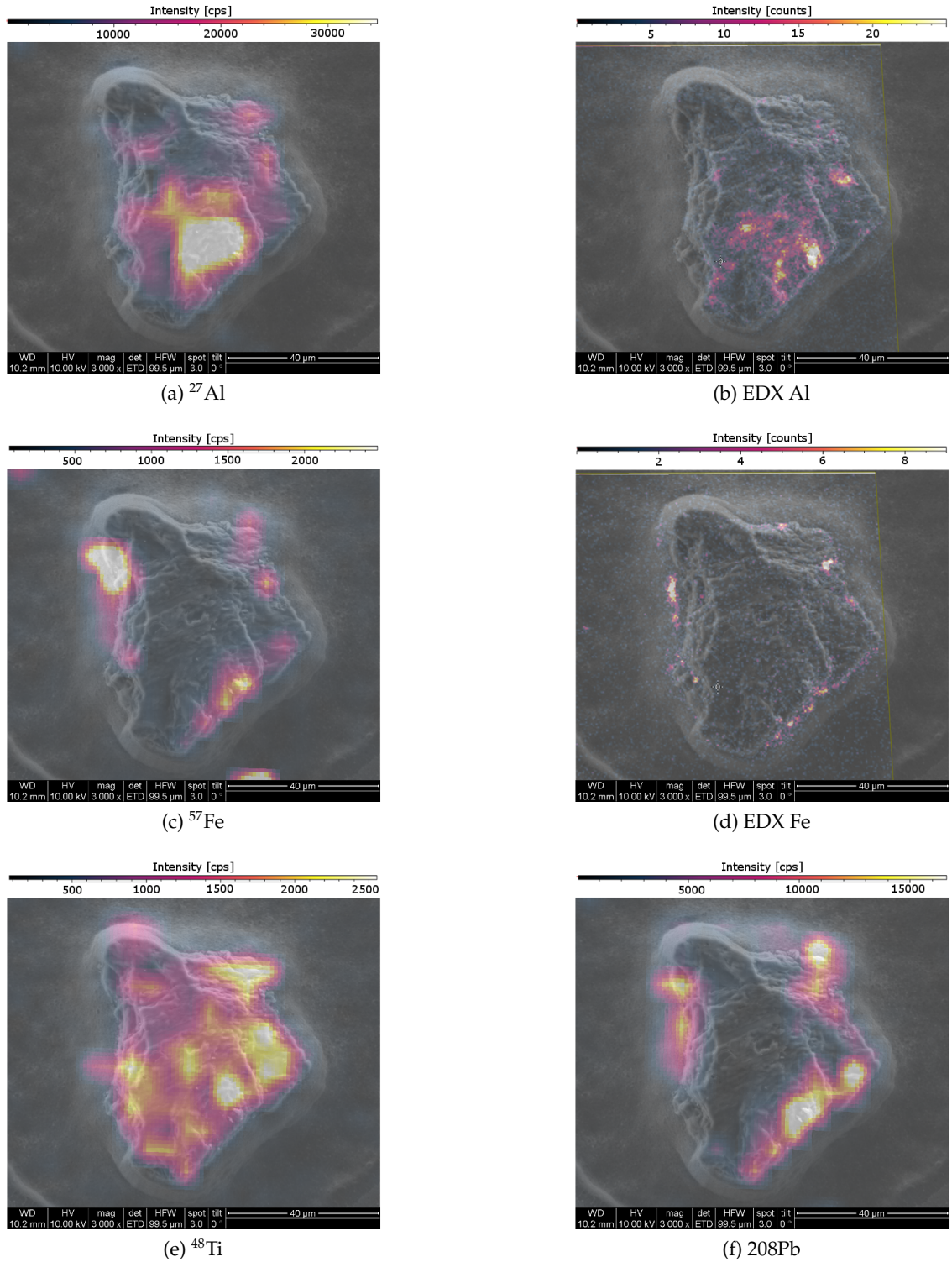


Figure 4.18: Comparison of elemental imaging using LA-ICP-MS and SEM-EDX, HZ9, Spot 9, Laser parameter: 50 %, 20 Hz, 5 μm , 3 $\mu\text{m sec}^{-1}$, 20.05.2015

4 Results and Discussion

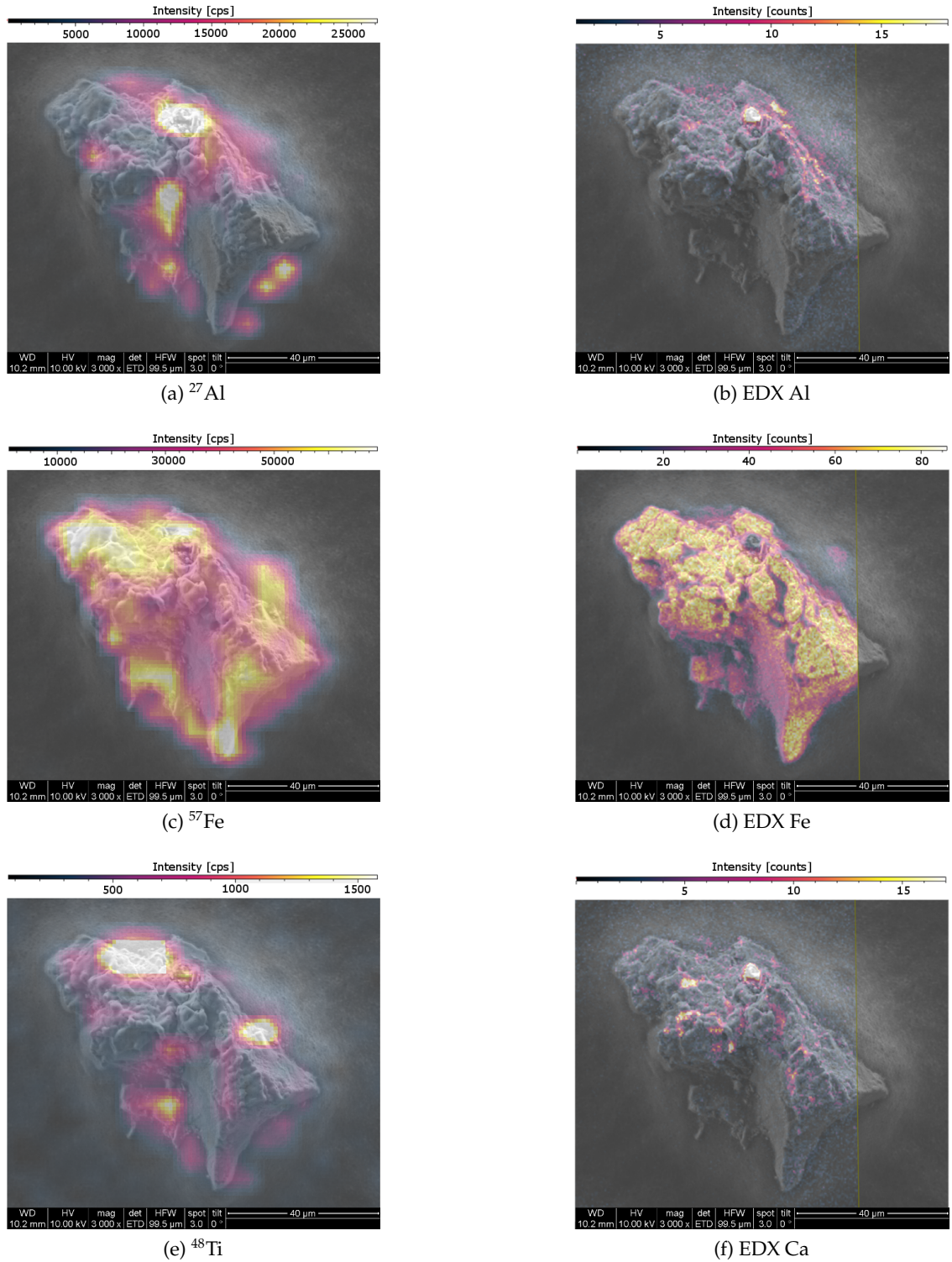


Figure 4.19: Comparison of elemental imaging using LA-ICP-MS and SEM-EDX, HZ9, Spot 7, Laser parameter: 50 %, 20 Hz, 5 μm , 3 $\mu\text{m sec}^{-1}$, 20.05.2015

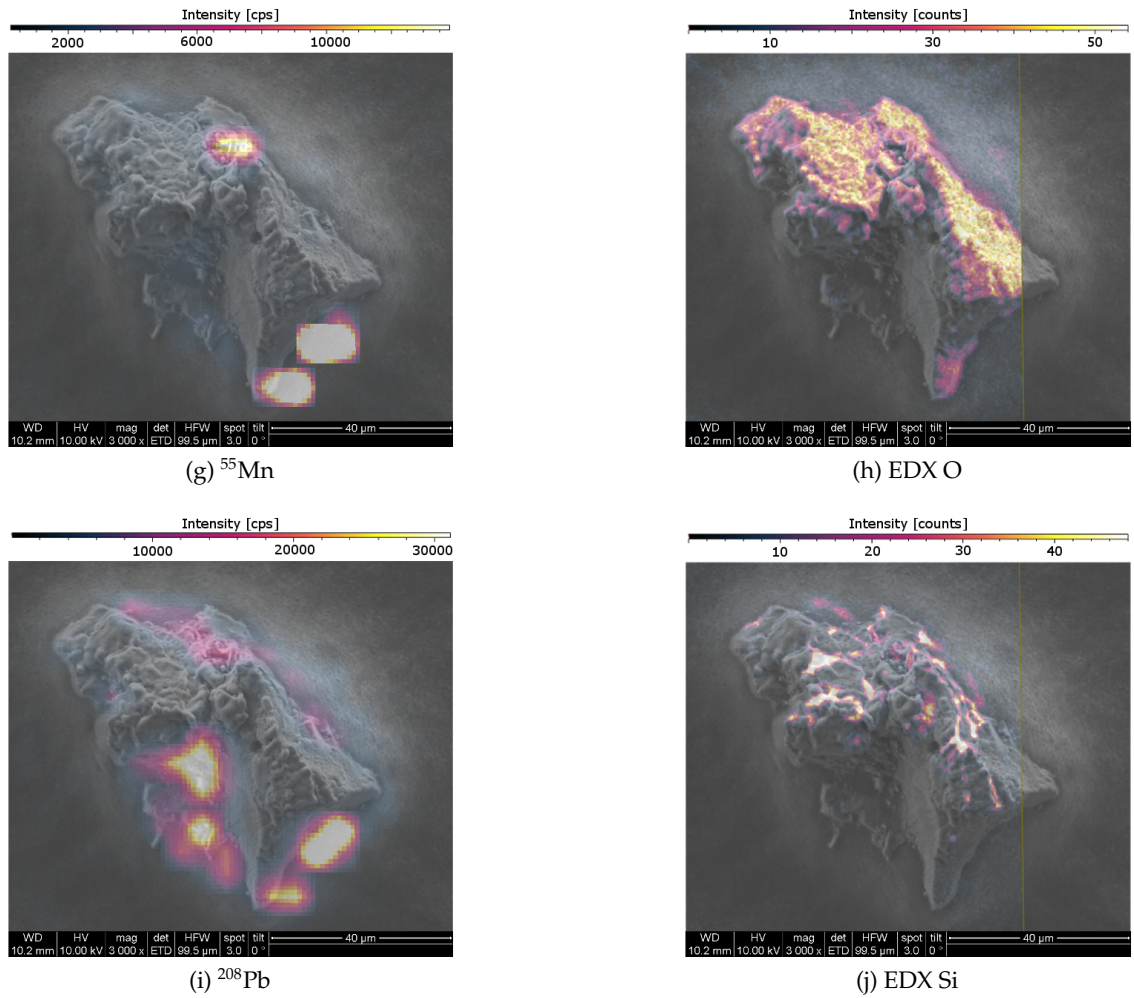


Figure 4.19: Comparison of elemental imaging using LA-ICP-MS and SEM-EDX, HZ9, Spot 7, Laser parameter: 50 %, 20 Hz, 5 μm , 3 $\mu\text{m sec}^{-1}$, 20.05.2015

5 Conclusion

During this work, characterization of fly ash samples was done using LA-ICP-MS and SEM-EDX measurements. Elemental images from both techniques were combined to obtain detailed analysis of a single particle.

Two samples from different sectors of industry were analyzed: FLA fly ash was sampled at a municipal waste incinerator (Spittelau, Vienna) and HZ9 fly ash was received from a blast furnace (voestalpine, Linz).

5.1 Method development and optimization

The first challenge was the development of a sample preparation strategy to capture isolated fly ash particles on a sample carrier and retain them during laser ablation or vacuum conditions in SEM. The representative application of all particle sizes was required as well as the capture of single, isolated particles. The subsequently performed experiments were only reasonable if particles with sizes accountable for the main portion of sample were analyzed. Additionally, investigations had to be performed without the occurrence of interferences from overlapping particles.

In order to dispense the fly ash samples a self-combined device, consisting of a standard ICP-MS cyclonic spray chamber and a custom made glass elbow piece, was developed. An applied Argon stream swirled up the particles and transferred them onto the surface of a prepared sample carrier. Tops and bottoms of petri dishes were designated as basis for particle fixation and were placed under the elbow piece.

Before sample application, the petri dish surfaces had been sputtered with gold and anti-static spray had been applied. The gold layer was necessary to distinguish between particle and mounting base during later performed LA-ICP-MS experiments. Anti-static spray served as a fixation media that offered enough adhesive strength to retain particles

but prevented them from overlapping. Several other fixation media were tested, such as hairspray and tape but were discarded soon. After fly ash application, hairspray was used to secure the sample. The so-prepared sample carriers were analyzed using optical microscopy to review the particle distribution and the ImageJ software to measure particle sizes.

Antistatic-spray as fixation media in combination with the application through the self-combined apparatus provided the best results. Compared to other fixation media and application techniques, adequate particle separation also in densely coated areas of the petri dish surface was received. Moreover, the particle size distribution calculated with the ImageJ software corresponded well with the measured particle size distribution from a Mastersizer 2000.

With the so-prepared samples, the analysis of single fly ash particles using LA-ICP-MS was allowed. First of all, a cross-section of a single specimen had to be obtained to allow the analysis of inner structures. That was done by removing the top section of a specimen with the laser. Ideally, one third to half of each particle ought to be removed which was impossible due to different shapes, orientation and composition of the fly ash. However, different compositions of core and shell were detectable at any cross-section.

The ablation was done using mild conditions, a low repetition rate and a beam diameter larger than the particle diameter to remove hairspray from the surrounding area. Mild conditions were executed to prevent alteration of the fly ash during pre-ablation and a low repetition rate was helpful during method optimization to visually observe the laser effect on the sample. In general, ten shots with a fluence of 3-4 J cm⁻² per particle were applied.

The analysis of a produced cross-section allowed further examination to determine the fly ash composition and elemental distribution. Two laser-based analysis methods were developed:

- Single linescan measurements were performed to monitor the existence of enriched structures in a fast and easy way.
- Imaging of the whole cross-section was done using several linescan pattern. With

the obtained data the generation of elemental mappings was facilitated.

The analyte selection for LA-ICP-MS investigations was done based on mass spectra obtained from a survey scan. During this measurement programme the whole mass spectrum was recorded while ablating FLA and HZ9 samples. The detected elements were classified into main and secondary analytes, depending on the signal intensity in the survey scan.

For a single linescan analysis a measurement pattern was placed at a user-defined position on the pre-ablated cross-section. The laser energy and beam diameter were optimized to reach sufficient ablation of material for main and secondary analytes while obtaining the highest possible resolution. As the petri dishes were coated with a thin gold layer during sample preparation, the isotope ^{197}Au was recorded to differentiate between particle and background. The optimized laser parameters for main analytes were set to a fluence of $5\text{--}6\text{ J cm}^{-2}$ corresponding to a $5\text{ }\mu\text{m}$ beam diameter for both fly ash samples. When recording secondary analytes the beam diameter was increased to $10\text{ }\mu\text{m}$. Considering FLA samples, the main analytes were ^{27}Al , ^{48}Ti , ^{66}Zn and ^{208}Pb . For HZ9 only ^{27}Al and ^{208}Pb were reliably detectable.

During single linescan analysis it was discovered that the obtained signal trends were depending on the position of the pattern within the cross-section. Therefore, only one measurement scan did not provide a representative result for the whole particle surface. Nevertheless, the detection of enriched structures was possible and core-shell distributions were detected. In general, Al was considered evenly distributed while Pb was found preferentially in outer particle areas. Enrichment of elements in the outer particle sphere was discovered in 13-14 % of FLA and 4-9% of HZ9 particles.

Imaging experiments were conducted to provide more detailed and most importantly space-resolved information about elemental distribution on a particle's surface. Main and secondary analytes were combined in one measurement cycle and the initial laser parameters from single linescan measurements were adjusted. A beam diameter of $5\text{ }\mu\text{m}$ and a fluence of $5\text{--}6\text{ J cm}^{-2}$ were considered standard settings. Experiments with a beam diameter of $3\text{ }\mu\text{m}$ and an adapted fluence of $17\text{--}18\text{ J cm}^{-2}$ provided significant data as well.

The recorded signal intensities from LA-ICP-MS were processed using the ImageLab software to generate elemental mappings of the scanned cross-section. As a result, the behavior of certain elements became visible. Although the content of main and trace components of a fly ash sample can be easily received through bulk analysis, spatial information was only obtained from the described experiments.

Finally, the development of a method validation strategy was necessary to verify the adjusted laser settings and the constructed elemental images. Hence, SEM (Secondary electron microscopy) was the method of choice and the analysis was done prior to laser-based investigations. SEM allowed the recording of pictures with high spatial resolution to gain insight into optical structures of fly ash particles. Moreover, it was possible to attach those pictures to the created elemental mappings in the ImageLab software. It was discovered that optical structures were reflected by the distribution of analytes on a cross-section.

Additionally, the identification and distribution of main components was possible through EDX measurements and a comparison of analytes accessible by both, LA-ICP-MS and x-ray spectroscopy, was done. It had to be kept in mind that during LA-ICP-MS several μm of material got ablated while during x-ray spectroscopy only the top atomic layers were excited. Although there is the potential risk of differing images, an overall good correspondence for both techniques was found. Comparable elements were limited to Al, Ti, Zn and Si for FLA samples and Al and Fe for HZ9 fly ash. However, LA-ICP-MS elemental distributions were verified and considered reliable.

SEM also enabled the investigation of impacts from laser treatment on the structure of a particle. The influence of enhanced fluence values was of particular concern. It was found that working with a fluence of $17 - 18 \text{ J cm}^{-2}$ when decreasing the beam diameter to $3 \mu\text{m}$ led to increased mass removal and nearly the whole particle got ablated. Although LA-ICP-MS experiments provided reasonable elemental distributions, the laser settings were discarded during further experiments.

By combining information from both techniques a precise analysis of a single particle was possible. SEM and EDX investigations provided insights into the structure of a

particle and allowed the identification of main elements and their distribution throughout a cross-section. Lesser concentrated analytes were measured using LA-ICP-MS. As real-life particles did not represent ideal spheres and adsorption and condensation took place on specific surface regions, classification into core-shell and non-core-shell particles seemed impracticable. It was found out that main components were evenly distributed while trace elements were enriched in specified particle structures.

5.2 Sample characterisation

FLA fly ash was collected from a municipal waste incinerator and various structural differences as well as a wide range of analytes were detected using LA-ICP-MS and SEM-EDX. All in all, 27 particles with sizes between 60 - 120 μm were analysed using both techniques.

Crumb-like arrangements, agglomerates of middle-sized, isolated particles and bigger, flat structures looking like melt were found to be the main structural components. Ca, O, Al, Si and to a lesser extent S and Mg were considered the main analytes.

Using EDX analysis, it was found out that Ca, O and S formed the basis of the particle and were present throughout the whole cross-section. Signal trends for ^{27}Al , ^{29}Si , ^{48}Ti , ^{63}Cu , ^{66}Zn , ^{120}Sn , ^{121}Sb and ^{208}Pb were provided by LA-ICP-MS imaging experiments. In most of the particles, Al and Si were widely distributed with punctual enrichments in molten-looking areas and smaller, isolated agglomerate structures. Ti turned out to be accumulated in certain, isolated particles while Cu, Zn, Sn, Sb and Pb showed similar elemental distributions. They were found primarily in crumb-like aggregates at the outer sphere of a particle.

In order to compare particle structures and the composition from samples obtained from different sectors of industry, HZ9 fly ash which was collected from a blast furnace at a steel producing company was analyzed as well. 10 particles were characterized using LA-ICP-MS and SEM-EDX measurements.

In general, HZ9 samples exhibited less complex structures and chemical components compared to FLA fly ash. Two main components, iron and soot were determined. Ad-

ditional elemental mappings were provided by LA-ICP-MS where signals for ^{27}Al , ^{48}Ti , ^{55}Mn , ^{66}Zn , ^{120}Sn and ^{208}Pb were recorded. Carbon-based particles showed enrichments of Al and Ti throughout the cross-section while traces of Fe were found at the border. Iron-based particles contained Fe, O, and little Ca and Si while enrichments of Ti, Mn, Zn, Sn and Pb were only found punctually at outer areas. In conclusion, it can be assumed that HZ9 fly ash particles originated from abrasion and adsorption or condensation of the other elements took place.

6 Outlook

LA-ICP-MS in combination with SEM-EDX provided a powerful tool to display the structure and elemental distribution of a single fly ash particle. Although a precise analysis was performed for selected particles, improvements in the measurement process and the sample characterization are possible.

During this work, the focus was laid on specimen sizes between 50 - 120 μm because both samples exhibited the maximum of the measured particle size distribution in this area. Nevertheless, method development for particles with sizes smaller than 50 μm would be interesting. Using the additional data, a comparison of particle properties of various sizes would be possible. The HZ9 sample also exhibited a bimodal particle size distribution with the second maximum at a particle diameter of 10 μm . To fully characterize this fly ash, an analysis of smaller particles is necessary.

Additionally, the measurement of environmentally relevant elements like Cr and Cd or precious metals of economic value would be of concern. To detect elements presumably present at very low concentrations was not possible during the performed experiments. To improve the detection limit in LA-ICP-MS the preferred strategy is to increase the amount of ablated material by elevated laser power or beam diameter. In order not to lose spatial resolution, the development of an additional measurement strategy would be required. Step-by-step ablation of a particle from top to bottom using a large beam diameter might be a possibility in the future.

Another interesting challenge would be the quantification of elemental distributions. In this context, it has to be kept in mind that the amount of mass removed by the laser depends on the particle structure especially when a specimen consists of an agglomerate of smaller and middle-sized particles. As a result, a quantification strategy for different

types of particle structure would have to be introduced.

Finally, solid waste is accumulated during every combustion process in several industries. Particularly fly ash is considered hazardous due to a high concentration of metals, soluble salts and toxic organic pollutants. Further usage is therefore often limited and deposition is expensive. By detailed characterisation of other solid residues, knowledge of structure, composition and behavior of elements is accumulated. Therefore, a comprehensive description of a solid residue is feasible and enables the development of a recycling strategy in the future.

Bibliography

- [1] A. Bogush, J. a. Stegemann, I. Wood, and A. Roy, "Element composition and mineralogical characterisation of air pollution control residue from UK energy-from-waste facilities," *Waste Management*, vol. 36, pp. 119–129, 2015.
- [2] B. Winter, H. Reisinger, and T. Janhsen, "Abfallvermeidung Schlacken und Stäube in Österreich," Tech. Rep., 2005.
- [3] H. Shen and E. Forssberg, "An overview of recovery of metals from slags," *Waste Management*, vol. 23, no. 10, pp. 933–949, 2003.
- [4] S. M. Shaheen, P. S. Hooda, and C. D. Tsadilas, "Opportunities and challenges in the use of coal fly ash for soil improvements – A review," *Journal of Environmental Management*, vol. 145, pp. 249–267, 2014.
- [5] C. H. K. Lam, A. W. M. Ip, J. P. Barford, and G. McKay, "Use of Incineration MSW Ash: A Review," *Sustainability*, vol. 2, no. 7, pp. 1943–1968, 2010.
- [6] Z. T. Yao, X. S. Ji, P. K. Sarker, J. H. Tang, L. Q. Ge, M. S. Xia, and Y. Q. Xi, "A comprehensive review on the applications of coal fly ash," *Earth-Science Reviews*, vol. 141, no. 0, pp. 105–121, 2015.
- [7] E. R. Teixeira, R. Mateus, A. F. Camões, L. Bragança, and F. G. Branco, "Comparative environmental life-cycle analysis of concretes using biomass and coal fly ashes as partial cement replacement material," *Journal of Cleaner Production*, pp. 1–10, 2015.
- [8] L. S. Morf, R. Gloor, O. Haag, M. Haupt, S. Skutan, F. D. Lorenzo, and D. Böni, "Precious metals and rare earth elements in municipal solid waste - Sources and fate in a Swiss incineration plant," *Waste Management*, vol. 33, no. 3, pp. 634–644, 2013.

- [9] J. Krook and L. Baas, "Getting serious about mining the technosphere: A review of recent landfill mining and urban mining research," *Journal of Cleaner Production*, vol. 55, pp. 1–9, 2013.
- [10] A. S. Meawad, D. Y. Bojinova, and Y. G. Pelovski, "An overview of metals recovery from thermal power plant solid wastes," *Waste Management*, no. 12, pp. 2548–2559, 2010.
- [11] R. Ibáñez, a. Andrés, J. R. Viguri, I. Ortiz, and J. a. Irabien, "Characterisation and management of incinerator wastes," *Journal of Hazardous Materials*, vol. 79, no. 3, pp. 215–227, 2000.
- [12] A. De Boom and M. Degrez, "Belgian MSWI fly ashes and APC residues: A characterisation study," *Waste Management*, vol. 32, no. 6, pp. 1163–1170, 2012.
- [13] H. Zhang, P.-J. He, and L.-M. Shao, "Fate of heavy metals during municipal solid waste incineration in Shanghai." *Journal of hazardous materials*, vol. 156, no. 1-3, pp. 365–373, 2008.
- [14] M. Xu, R. Yan, C. Zheng, Y. Qiao, J. Han, and C. Sheng, "Status of trace element emission in a coal combustion process: A review," *Fuel Processing Technology*, vol. 85, pp. 215–237, 2004.
- [15] D. H. Klein, A. W. Andren, J. a. Carter, J. F. Emery, C. Feldman, W. Fulkerson, W. S. Lyon, J. C. Ogle, Y. Talmi, R. I. V. Hook, and N. Bolton, "Pathways of Thirty-seven Trace Elements Through Coal-Fired Power Plant," *October*, vol. 9, no. 10, pp. 973–979, 1975.
- [16] M. Fernandez, L. Martinez, M. Segarra, J. C. Garcia, and F. Espiell, "Behavior of Heavy Metals in the Combustion Gases of Urban Waste Incinerators," *Society*, vol. 26, no. 5, pp. 1040–1047, 1992.
- [17] C.-H. Jung and M. Osako, "Metal resource potential of residues from municipal solid waste (MSW) melting plants," *Resources, Conservation and Recycling*, vol. 53, no. 6, pp. 301–308, 2009.

- [18] —, "Thermodynamic behavior of rare metals in the melting process of municipal solid waste (MSW) incineration residues," *Chemosphere*, vol. 69, no. 2, pp. 279–288, 2007.
- [19] J. S. Becker, *Inorganic Mass Spectrometry*. Chichester, UK: John Wiley & Sons, Ltd, dec 2007.
- [20] Universiteit Gent, "Universiteit Gent - Department of Analytical Chemistry," visited on 2015-10-02. [Online]. Available: http://www.analchem.ugent.be/ams_onderzoek_solid/index.php?language=EN
- [21] A. Montaser, *Inductively Coupled Plasma Mass Spectrometry*. John Wiley & Sons, Ltd, 1998.
- [22] R. E. Russo and X. Mao, "Chemical Analysis by Laser Ablation," *Experimental methods in the physical sciences*, vol. 30, pp. 375–412, 1998.
- [23] D. Barshick, Christopher Duckworth and D. Smith, *Inorganic Mass Spectrometry: Fundamentals and Applications*. CRC Press, 2000.
- [24] Robert Thomas, *Practical Guide to ICP-MS: A Tutorial for Beginners (Second Edition)*. Crc Pr Inc, 2008.
- [25] H. Lohninger, J. Fröhlich, B. Mizaikoff, and E. Rosenberg, *Teach/Me Instrumentelle Analytik*. Springer, 2003. [Online]. Available: <http://teachme.tuwien.ac.at/tmanalytik/>
- [26] R. E. Russo, X. Mao, H. Liu, J. Gonzalez, and S. S. Mao, "Laser ablation in analytical chemistry-a review." *Talanta*, vol. 57, no. 3, pp. 425–451, 2002.
- [27] D. Günther and B. Hattendorf, "Solid sample analysis using laser ablation inductively coupled plasma mass spectrometry," *TrAC - Trends in Analytical Chemistry*, vol. 24, no. 3 SPEC. ISS., pp. 255–265, 2005.
- [28] N. Omenetto, "Role of lasers in analytical atomic spectroscopy : where , when and why † Plenary Lecture," *Techniques*, vol. 13, no. May, pp. 385–399, 1998.
- [29] J. C. Miller, "A brief history of laser ablation," *AIP Conference Proceedings*, vol. 288, no. 1, p. 619, 1993.

- [30] J. Koch and D. Günther, "Review of the State-of-the-Art of Laser Ablation Inductively Coupled Plasma Mass Spectrometry," *Applied Spectroscopy*, vol. 65, no. 5, pp. 155–162, 2011.
- [31] G. C.-Y. Chan, W. Chan, X. Mao, and R. E. Russo, "Investigation of matrix effect on dry inductively coupled plasma conditions using laser ablation sampling," *Spectrochimica Acta Part B: Atomic Spectroscopy*, vol. 55, pp. 221–235, 2000.
- [32] J. J. Gonzalez, A. Fernandez, D. Oropeza, X. Mao, and R. E. Russo, "Femtosecond laser ablation: Experimental study of the repetition rate influence on inductively coupled plasma mass spectrometry performance," *Spectrochimica Acta Part B: Atomic Spectroscopy*, vol. 63, no. 2, pp. 277–286, 2008.
- [33] D. Waller, L. G. Coccia, J. A. Kilner, and I. W. Boyd, *Laser Ablation*. Elsevier B.V., 2000, vol. 134.
- [34] J. D. Winefordner, I. B. Gornushkin, D. Pappas, O. I. Matveev, and B. W. Smith, "Novel uses of lasers in atomic spectroscopy," *Journal of Analytical Atomic Spectrometry*, vol. 15, no. 9, pp. 1161–1189, 2000.
- [35] Z. Wang, B. Hattendorf, and D. Günther, "Analyte response in laser ablation inductively coupled plasma mass spectrometry," *Journal of the American Society for Mass Spectrometry*, vol. 17, no. 5, pp. 641–651, 2006.
- [36] J. J. González, A. Fernández, X. Mao, and R. E. Russo, "Scanning vs. single spot laser ablation ($\lambda = 213$ nm) inductively coupled plasma mass spectrometry," *Spectrochimica Acta - Part B Atomic Spectroscopy*, vol. 59, no. 3, pp. 369–374, 2004.
- [37] S. L. Flegler, J. W. Heckman, and K. L. Klomparens, *Elektronenmikroskopie: Grundlagen, Methoden, Anwendungen*. Spektrum Akademischer Verlag, 1995.
- [38] TU München - Fakultät für Chemie, "Rasterelektronenmikroskopie (REM)," visited on 2015-10-09. [Online]. Available: <http://www.zentralanalytik.ch.tum.de/index.php?id=357>
- [39] J. I. Goldstein, D. E. Newbury, P. Echlin, D. C. Joy, C. E. Lyman, E. Lifshin, L. Sawyer,

- and J. R. Michael, *Scanning Electron Microscopy and X-ray Microanalysis*, 3rd ed. Boston, MA: Springer US, 2003.
- [40] L. Reimer, *Scanning Electron Microscopy*, ser. Springer Series in Optical Sciences. Berlin, Heidelberg: Springer Berlin Heidelberg, 1998, vol. 45.
- [41] R. Kellner, J.-M. Mermet, M. Otto, M. Valcarcel, and H. M. Widmer, *Analytical Chemistry: A Modern Approach to Analytical Science*, 2nd ed. Wiley-VCH Verlag GmbH & Co. KGaA, 2004.
- [42] Thermo Scientific, “iCAPTM Q ICP-MS,” visited on 2015-10-14. [Online]. Available: <http://www.thermoscientific.com/content/tfs/en/product/icap-q-icp-ms.html>
- [43] ESI, “NWR213 Laser Ablation System,” visited on 2015-10-14. [Online]. Available: <http://www.esi.com/Products/LaserAblation/NWR213.aspx>
- [44] M. Bonta, H. Lohninger, M. Marchetti-Deschmann, and A. Limbeck, “Application of gold thin-films for internal standardization in LA-ICP-MS imaging experiments,” *Analyst*, vol. 139, pp. 1521–1531, 2014.
- [45] S. Smetaczek, “Entwicklung eines Analyseverfahrens für die Untersuchung isolierter Partikel mittels LA-ICP-MS,” Tech. Rep., 2014.

List of Figures

2.1	Formation of solid residues within the waste incineration process [2] . . .	5
2.2	Principal components of a quadrupole ICP-MS system [20]	9
2.3	Schematic of an inductively coupled plasma source and interface region [19]	11
2.4	Schematic illustration of a quadrupole mass filter [25]	15
2.5	Schematic set-up of LA-ICP-MS [27]	18
2.6	Schematic set-up of a SEM [39]	22
2.7	Information depth of secondary electrons (SE), backscattered electrons (BSE), Auger electrons (AE) and characteristic radiation (X).[40]	24
2.8	Image creation using secondary electrons (SE)[37]	25
3.1	Equipment used for performed experiments	26
3.2	Device for sample dispersal	29
3.3	Schematic illustration of sample preparation	29
3.4	Schematic illustration of the pre-ablation procedure	30
3.5	Schematic illustration of a linescan measurement	31
3.6	Schematic illustration of an image measurement	32
4.1	Comparison of different mounting media (a) anti-static spray , (b) hair- spray (c) tape	35
4.2	Particle distribution obtained on the surface of a petri dish (a) particle arrangement in the densely coated area in the middle of the sample carrier, (b) schematic of the appearance of a sampled petri dish surface, (c) particle arrangement outside the densely coated area in the middle of the sample carrier	36
4.3	Particle size distribution of a section of (19)_HZ9_<0,5bar_A	37
4.4	Transformation of a FLA fly ash particle during pre-ablation	39

List of Figures

4.5	Survey scan mass spectrum for one particle of (a) FLA and (b) HZ9 fly ash	40
4.6	Linescan optimization on (17)_HZ9<0.5bar_A (Spot 7, 04.02.2015)	43
4.7	Schematic of a linescan pattern used to analyze single particles	44
4.8	(14)_FLA_0.5bar_A (Spot 12, 26.02.2015)	45
4.9	(14)_FLA_0.5bar_A (Spot 10, 19.02.2015)	46
4.10	(17)_HZ9<0.5bar_A (27.02.2015)	48
4.11	Evaluated imaging experiment using ImageLab software, (17)_HZ9<0.5bar_A, Spot 7, Laser parameter: 80 %, 20 Hz, 3 μm , 3 $\mu\text{m sec}^{-1}$, 22.04.2015	51
4.12	Pictures from selected FLA fly ash particles obtained from secondary electrons (SE), sample (14)_FLA_0.5bar_A	53
4.13	Pictures from selected HZ9 fly ash particles obtained from secondary electrons (SE), sample (17)_HZ9<0.5bar_A	54
4.14	Comparison of elemental imaging using LA-ICP-MS and SEM-EDX, FLA, Spot 8, Laser parameter: 60 %, 20 Hz, 3 μm , 3 $\mu\text{m sec}^{-1}$, 05.05.2015	56
4.15	Pictures from selected fly ash particles obtained from secondary electrons (SE) after laser treatment	57
4.16	Comparison of elemental imaging using LA-ICP-MS and SEM-EDX, FLA, Spot 2, Laser parameter: 50 %, 20 Hz, 5 μm , 3 $\mu\text{m sec}^{-1}$, 15.04.2015	60
4.16	Comparison of elemental imaging using LA-ICP-MS and SEM-EDX, FLA, Spot 2, Laser parameter: 50 %, 20 Hz, 5 μm , 3 $\mu\text{m sec}^{-1}$, 15.04.2015	61
4.17	Comparison of elemental imaging using LA-ICP-MS and SEM-EDX, FLA, Spot 3, Laser parameter: 80 %, 20 Hz, 3 μm , 3 $\mu\text{m sec}^{-1}$, 15.04.2015	62
4.17	Comparison of elemental imaging using LA-ICP-MS and SEM-EDX, FLA, Spot 3, Laser parameter: 80 %, 20 Hz, 3 μm , 3 $\mu\text{m sec}^{-1}$, 15.04.2015	63
4.18	Comparison of elemental imaging using LA-ICP-MS and SEM-EDX, HZ9, Spot 9, Laser parameter: 50 %, 20 Hz, 5 μm , 3 $\mu\text{m sec}^{-1}$, 20.05.2015	65
4.19	Comparison of elemental imaging using LA-ICP-MS and SEM-EDX, HZ9, Spot 7, Laser parameter: 50 %, 20 Hz, 5 μm , 3 $\mu\text{m sec}^{-1}$, 20.05.2015	66
4.19	Comparison of elemental imaging using LA-ICP-MS and SEM-EDX, HZ9, Spot 7, Laser parameter: 50 %, 20 Hz, 5 μm , 3 $\mu\text{m sec}^{-1}$, 20.05.2015	67

List of Tables

3.1	Laser ablation system measurement parameters	27
3.2	ICP-MS measurement parameters	27
3.3	Laser parameters for linescan measurements	31
3.4	Laser parameters for imaging with LA-ICP-MS	32
4.1	Experimental parameters for sample preparation	35
4.2	Experimental parameters for pre-ablation	39
4.3	Results from several survey scans for HZ9 and FLA samples	41
4.4	Original linescan parameters	41
4.5	Linescan measurement statistics	47
4.6	Tested laser conditions during LA-ICP-MS imaging experiments	50
4.7	Comparable analyte signals from LA-ICP-MS and EDX	54